Atmospheric Research 344 (2027) 109312

Contents lists available at ScienceDirect

Atmospheric Research

journal homepage: www.elsevier.com/locate/atmosres

Quantifying the aging of dust aerosols using Mie–polarization–fluorescence lidar: Linking optical evolution to chemical transformations

Yuanzong Ji [a], Zhongwei Huang [a,b,*], Yongkai Wang [a], Wenjin Zhang [a], Da Lu [a], Qingqing Dong [a], Jianrong Bi [a,b], Tian Zhou [a,b]

[a] Key Laboratory for Semi-Arid Climate Change of the Ministry of Education, College of Atmospheric Sciences, Lanzhou University, Lanzhou 730000, China
[b] Collaborative Innovation Center for West Ecological Safety (CIWES), Lanzhou University, Lanzhou 730000, China

ARTICLE INFO

Keywords:
Fluorescence lidar
Dust aerosol
Fluorescence spectrum
Dust aging index (DAI)
Ion chromatography
Particle size distribution

ABSTRACT

Dust particles undergo complex physical and chemical aging processes during long-range atmospheric transport, substantially altering their optical properties and environmental impacts. However, real-time quantification of dust aging and its vertical evolution remains challenging. In this study, a Mie scattering–polarization–fluorescence lidar combined with ground-based measurements was used to investigate dust mixing and aging over Northwest China. A novel Dust Aging Index (DAI) was developed by integrating multiple optical parameters to quantitatively characterize the mixing process and aging state of dust aerosols. Stage-dependent variations in fluorescence spectra reflected systematic compositional changes during aging. During fresh dust mixing, fluorescence was dominated by short-wavelength emissions; however, as external mixing and aging progressed, the spectral peak shifted towards longer wavelengths, reflecting an increasing contribution from highly oxidized organic compounds. The DAI exhibited a pronounced non-monotonic evolution, indicating that dust aging proceeded through multiple transitional stages rather than a simple linear progression. Before the arrival of the principal dust plume, the DAI remained comparatively high, attaining 0.43. Following the intrusion of fresh mineral dust, the DAI decreased to 0.32 before gradually increasing to 0.42 during subsequent chemical aging. Further analyses integrating ion chromatography and particle size distribution measurements revealed a strong association between long-wavelength fluorescence emissions, submicron particles, and secondary aerosol precursors, suggesting that dust aging facilitated the formation and accumulation of oxidized organic matter. This study provides a novel remote-sensing framework for quantifying dust aging and advances our understanding of the evolving impacts of atmospheric dust on climate, environment, and human health.

1. Introduction

Atmospheric aerosols comprise solid and liquid particles suspended within the atmosphere. They exert substantial influences on the Earth's radiation balance, climate, hydrological processes, and air quality through aerosol–radiation and aerosol–cloud interactions (Kok et al., 2023; Adebiyi et al., 2023). Mineral dust originating from arid and semi-arid regions constitutes the largest contributor to the global atmospheric aerosol burden, with annual emissions estimated to range from 1 to 3 billion tonnes. Long-range transport of mineral dust plays a crucial role in global biogeochemical cycling by delivering essential nutrients to terrestrial and marine ecosystems, including the Amazon rainforest (Wang et al., 2023a; Li and Wang, 2024; Zan et al., 2025). However, dust transport can also degrade air quality and adversely affect human health, infrastructure, and socioeconomic activities.

During atmospheric transport, dust particles continuously interact with a variety of atmospheric pollutants, including sulfur oxides, nitrogen oxides, volatile organic compounds, black carbon (BC), brown carbon (BrC), and biomass-burning aerosols (Zhang et al., 2008; Shen et al., 2013; Tang et al., 2017; Wang et al., 2017). These interactions modify particle morphology, chemical composition, hygroscopicity, and optical characteristics through a series of physical and chemical transformations collectively referred to as dust aging (Gaston, 2020; Li et al., 2023a, 2023b; Liu et al., 2025). Fresh dust particles are generally hydrophobic; however, following atmospheric aging, they become increasingly hydrophilic owing to the accumulation of sulfate and

* Corresponding author at: Key Laboratory for Semi-Arid Climate Change of the Ministry of Education, College of Atmospheric Sciences, Lanzhou University, Lanzhou 730000, China.
E-mail address: huangzhongwei@lzu.edu.cn (Z. Huang).

https://doi.org/10.1016/j.atmosres.2026.109312
Received 15 July 2026; Received in revised form 24 August 2026; Accepted 3 September 2026
Available online 5 September 2026

nitrate coatings, thereby enhancing their ability to act as cloud condensation nuclei (CCN) and ice nuclei (IN) (Zhang et al., 2008; Miyamoto et al., 2020; Klingmüller et al., 2020; Casquero-Vera et al., 2023). Furthermore, mixing with light-absorbing aerosols such as BC and BrC can enhance shortwave radiation absorption and alter the single-scattering albedo (SSA), thereby potentially shifting the radiative effects of dust from net cooling to net warming (Klingmüller et al., 2020; Haywood et al., 2021; Zhang et al., 2021a, 2021b). In addition, dust aging progressively transforms irregularly shaped particles into more spherical morphologies, thereby significantly influencing their scattering and polarization characteristics (Pan et al., 2017; Tian et al., 2018; Yao et al., 2026).

Real-time, vertically resolved monitoring of dust aging remains a significant scientific and observational challenge. Ground-based measurements provide detailed and accurate chemical and microphysical information; however, their ability to characterize the vertical structure and regional distribution of dust aerosols is inherently limited (Song et al., 2013; Geng et al., 2014). Satellite observations provide extensive spatial coverage; however, their temporal continuity and capability to resolve vertical aerosol distributions remain limited (Ackerman, 1997; Legrand et al., 2001). Consequently, there is an urgent need for advanced remote-sensing techniques capable of providing real-time, in-situ quantification of dust aging. Lidar has become an indispensable tool for aerosol monitoring owing to its high temporal and spatial resolution and its ability to retrieve detailed vertical profiles of the atmosphere (Sugimoto et al., 2015; Wang et al., 2023b; Huang et al., 2025b). Conventional Mie lidar systems retrieve aerosol backscatter and extinction coefficients, whereas polarization lidar systems discriminate between spherical and non-spherical particles using depolarization ratios (Jing et al., 2024; Yadav et al., 2025). Previous studies have demonstrated that dust aging leads to reduced depolarization ratios, primarily because the accumulation of pollutant coatings progressively smooths particle surfaces and decreases particle irregularity (Groß et al., 2015; Pan et al., 2017; Yu et al., 2018; Yao et al., 2026). However, polarization- and scattering-based measurements primarily reflect changes in particle morphology and optical structure and are generally less sensitive to the chemical transformations associated with dust aging.

Laser-induced fluorescence (LIF) has emerged as a promising technique for the identification and characterization of aerosol components. Organic and biological aerosols exhibit characteristic fluorescence signatures when excited by laser radiation, enabling their detection and differentiation based on spectral features (Pan et al., 2014; Richardson et al., 2019; Huang et al., 2025a). Fluorescence properties of aerosol particles can vary with their organic composition and degree of atmospheric processing, providing complementary information to conventional scattering and polarization measurements. During long-range atmospheric transport, dust particles can acquire fluorescent constituents through interactions and mixing with polluted air masses and biological aerosol layers (Sugimoto et al., 2012a, 2012b; Reichardt et al., 2025). More importantly, atmospheric aging processes, including oxidation and nitration reactions, can induce systematic shifts in fluorescence emission peaks towards longer wavelengths. Similar fluorescence redshift phenomena have been widely documented in BrC, melanin, nitrogen-containing chromophores, and biogenic secondary organic aerosols (SOA) undergoing atmospheric aging; Wong(Bones et al., 2010; Fan et al., 2020; Lee et al., 2014; Ng et al., 2017; Pöhlker et al., 2012; Qin et al., 2022; Santos et al., 2009; Wong et al., 2024; Xie et al., 2016; Zhang et al., 2021a). Collectively, these findings suggest that fluorescence redshift has the potential to provide complementary optical information on the atmospheric processing of fluorescent organic components associated with dust-containing aerosol populations.

Building upon this concept, this study proposes a comprehensive remote-sensing parameter, termed the Dust Aging Index (DAI), to quantitatively characterize the mixing process and aging state of dust aerosols. To achieve this objective, a multi-channel lidar system integrating scattering, polarization, and fluorescence measurements was employed (Wang et al., 2023b; Huang et al., 2025a). The system simultaneously retrieves aerosol extinction coefficients, volume depolarization ratios, and fluorescence spectral information using an integrated 32-channel spectrometer. By integrating these complementary optical parameters, the DAI is designed to dynamically characterize the progression of dust aging from freshly emitted particles to more chemically processed aerosol populations. In addition, an ion chromatograph was used to quantify secondary inorganic ions and precursor gases associated with dust aging, while a particle size spectrometer continuously monitored aerosol size distributions. Correlation analyzes between the DAI and in situ measurements were conducted to evaluate the robustness and reliability of the proposed methodology. Overall, this study presents a novel lidar-based framework for real-time, in-situ, and vertically resolved monitoring of dust mixing and aging through the integrated analysis of scattering, polarization, and fluorescence observations.

2. Instruments and methods

2.1. Mie scattering–polarization–fluorescence lidar

The dust observation campaign was conducted from 25 to 26 March 2025 using a ground-based Mie scattering–polarization–fluorescence lidar system at Lanzhou University, China. The system primarily acquired 532 nm backscatter signals and fluorescence backscattering signals excited by a 355 nm laser source. The 532 nm backscatter signal was detected by two photomultiplier tubes (PMTs) after passing through a polarization beam-splitting crystal. The fluorescence detection subsystem integrated a grating spectrometer with a 32-channel PMT array, providing a spectral resolution of 5.8 nm. The detected fluorescence spectrum provided continuous spectral coverage over the wavelength range of 372–551 nm (Huang et al., 2025a). To minimize interference from Raman scattering by major atmospheric constituents, including O_2, N_2, and H_2O, and to avoid uncertainties associated with reduced signal reliability at the spectral boundaries, the effective fluorescence spectral range was restricted to 420–500 nm. The fluorescence measurements were recorded with temporal and spatial resolutions of 2 min and 15 m, respectively, whereas the corresponding temporal and spatial resolutions of the backscatter measurements were 5 min and 3.75 m, respectively. The raw lidar signals were sequentially processed through background subtraction, range-squared correction, geometric overlap correction, and polarization correction prior to subsequent analysis (Freudenthaler et al., 2009; Wang et al., 2018b; Li et al., 2019; Wang et al., 2023b). Owing the substantial influence of solar background radiation on weak fluorescence signals, fluorescence measurements were conducted exclusively during nighttime periods.

The purpose of the fluorescence measurements in this study was to characterize wavelength-dependent variations in the bulk fluorescent aerosol signal rather than to achieve molecular-level identification of individual fluorophores. Accordingly, the 420–500 nm range was used to investigate relative spectral evolution, including changes in peak position, spectral intensity, and spectral broadening.

2.2. Particle sizer and ion chromatograph

The TSI Scanning Mobility Particle Sizer (SMPS) is a high-resolution aerosol spectrometer designed to accurately measure the size distribution of submicron particles based on their electrical mobility characteristics. By integrating electrical mobility classification with particle-counting measurements, the SMPS determines particle number concentrations across a series of discrete size channels (Nannu Shankar et al., 2023; Lu et al., 2024). In this study, the SMPS was employed to monitor temporal variations in the number concentrations of atmospheric particles with diameters ranging from 9 to 371 nm throughout the dust event.

The concentrations of water-soluble ions and gaseous species were

measured using a high-performance ion chromatograph deployed at the Atmospheric Composition Supersite of Lanzhou University. The ion chromatograph separates ionic species through reversible ion-exchange processes occurring between charged functional groups on the resin and analyte ions of the same type present in the mobile phase. Differences in the affinity of individual ions for the exchange resin result in distinct retention behaviors, thereby enabling the quantitative determination of water-soluble ions and selected gaseous species (Meng et al., 2024; Wang et al., 2024).

2.3. Lidar data processing

Owing to the substantial influence of solar background radiation on weak fluorescence signals, fluorescence observations were conducted exclusively during nighttime periods. Because individual fluorescence detection channels exhibit different spectral response sensitivities, the spectrometer data were calibrated prior to subsequent analysis to ensure measurement consistency and spectral comparability (Reichardt et al., 2023). The standard lidar equation used to describe the received atmospheric backscatter signal is given in Eq. (1) (Ansmann et al., 1992), this equation provides the general theoretical basis for describing the propagation and attenuation of the received lidar signal:

$$P_S(r) = C\frac{P_0}{r^2}O(r)\beta(r)exp\left(-2\int_0^r \alpha(r')dr'\right) + P_b \tag{1}$$

here, P_0 and $P_S(r)$ represent the emitted laser power and the received backscatter signal intensity, respectively; r denotes the distance between the lidar and the target aerosol particles; C is the lidar system constant; and $O(r)$ represents the geometric overlap factor. β and α denote the aerosol backscatter coefficient and extinction coefficient, respectively. P_b represents the background signal, which includes contributions from ambient radiation and instrumental noise. Here, P_b was estimated from the lidar returns above 12 km, where the atmospheric aerosol contribution is negligible, and was subsequently subtracted from the low-altitude lidar signals. The background-corrected signal was then used for the subsequent retrieval. The normalized fluorescence intensity can be retrieved from the ratio of the fluorescence signal to the nitrogen Raman backscatter signal (Veselovskii et al., 2020). In this study, the ratio of the fluorescence signal to the nitrogen Raman scattering signal at 387 nm was used as the normalized fluorescence intensity parameter, as defined in Eqs. (2) and (3). The nitrogen Raman scattering signal and the fluorescence signals at different wavelengths can be expressed as follows (Veselovskii et al., 2020; Wang et al., 2023b):

$$P_{N_2}(r) = CP_0O(r)\beta_{N_2}\exp\left\{-\int_0^r [\alpha_0(r') + \alpha_{N_2}(r')]dr'\right\} \tag{2}$$

$$P_F(\lambda, r) = CP_0O(r)\beta_F\exp\left\{-\int_0^r [\alpha_0(\lambda, r') + \alpha_F(\lambda, r')]dr'\right\} \tag{3}$$

For the present lidar system, the system constant C in Eq. (1) can be further expressed in terms of the relevant instrumental parameters as follows:

$$P(r) = \frac{1}{2}KP_0c\tau\frac{A}{r^2}O(r)\beta(r)\exp\left[-2\int_0^r \alpha(r')dr'\right] \tag{4}$$

where K represents the overall system efficiency, c denotes the speed of light ($m{\cdot}s^{-1}$), τ represents the laser pulse duration (s) and A is the effective receiving area of the telescope. For the Fernald inversion, the aerosol extinction-to-backscatter ratio (lidar ratio) is defined as (Fernald, 1984):

$$S_A = \frac{\alpha_A(r)}{\beta_A(r)} \tag{5}$$

In this study, S_A was assumed to be 50 sr based on Huang et al. (2023). The corrected lidar signal was then inverted using the Fernald method, which separately accounts for the scattering contributions from aerosols and atmospheric molecules (Fernald, 1984; Welton and Campbell, 2002). An altitude of 10 km was selected as the reference height, where the aerosol contribution was assumed to be negligible. Using the prescribed aerosol lidar ratio and this reference condition, the aerosol backscatter coefficient was retrieved, and the corresponding aerosol extinction coefficient was subsequently calculated.

$$VDR = \frac{P_\perp}{P_\parallel} \tag{6}$$

After passing through a polarizing beam splitter (PBS), the 532 nm backscatter signal was separated into perpendicular and parallel polarization components. The ratio of these two components is defined as the volume depolarization ratio (VDR) (Eq. (6)), which is widely used to discriminate between spherical and non-spherical particles and is particularly effective for detecting morphology-related changes associated with dust aging (Liu et al., 2002; Sugimoto and Lee, 2006; Haarig et al., 2018).

2.4. Definition of dust aging index

Freshly emitted dust particles are typically irregular in shape and consequently exhibit relatively high depolarization ratios. During atmospheric aging, hygroscopic growth and the accumulation of surface coatings progressively transform dust particles towards more spherical morphologies, resulting in reduced volume depolarization ratios (Sakai et al., 2010). At different stages of atmospheric aging, variations in the abundance, composition, and chemical transformation of organic and biomass-derived materials associated with dust surfaces give rise to distinct fluorescence responses across different wavelength bands (Zhang et al., 2013; Pan, 2015). Therefore, based on observations acquired by the Mie scattering–polarization–fluorescence lidar, a multi-parameter DAI was developed by integrating information on particle nonsphericity (volume depolarization ratio), fluorescence spectral evolution (fluorescence measurements), and aerosol loading (extinction coefficient).

The volume depolarization-ratio sub-index (I_{VDR}) was introduced to characterize changes in the atmospheric processing state of dust-containing aerosol populations. Fresh dust particles generally exhibit high volume depolarization ratios; therefore, the upper threshold was defined as 0.35 ($VDR_{fre} = 0.35$). Following atmospheric aging, the volume depolarization ratio decreases owing to particle coating formation and morphological evolution; accordingly, the lower threshold was defined as 0.10 ($VDR_{old} = 0.10$). If VDR_{obs} represents the observed volume depolarization ratio, values calculated using Eq. (7) that approach 1 indicate a greater degree of dust aging, whereas values approaching 0 indicate fresh dust with limited atmospheric processing. It should be noted that $VDR_{old} = 0.10$ is consistent with a contribution from non-spherical particles and provides supporting evidence for the presence of dust. However, such a value is not unique to dust and may also occur in urban or smoke-influenced aerosol populations. Therefore, the VDR was interpreted together with the Mie-scattering and fluorescence measurements and other aerosol observations rather than being used as a standalone criterion for dust identification.

$$I_{VDR} = \frac{(VDR_{fre} - VDR_{obs})}{(VDR_{fre} - VDR_{old})} \tag{7}$$

The extinction-coefficient sub-index (I_{exco}) was introduced as an auxiliary parameter to characterize the aging state of dust aerosols. During the passage of the main dust plume, aerosol concentrations increase substantially, and the aerosol population becomes dominated by coarse-mode mineral dust particles that largely retain the physicochemical characteristics of their crustal source materials (Sugimoto and Lee, 2006; Sugimoto et al., 2016; Tesche et al., 2009). As a fundamental aerosol optical property, the extinction coefficient is strongly influenced

by particle number concentration, size distribution, and particle optical characteristics, particularly in the presence of coarse-mode aerosols (Papetta et al., 2025). During atmospheric transport and aging, processes such as gravitational settling, hygroscopic growth, and mixing with anthropogenic pollutants modify aerosol size distributions and particle number concentrations, thereby altering the extinction coefficient (Ansmann et al., 2003; Weinzierl et al., 2009). However, these changes do not necessarily follow a monotonic trend throughout the aging process. Because the extinction coefficient reflects aerosol loading and is also affected by changes in particle size distribution, transport, gravitational settling, dilution, and mixing, it was included as an auxiliary optical descriptor of the evolving aerosol population. The extinction coefficient was normalized to construct an extinction-based sub-index (I_{exco}), where E_{max} represents the maximum extinction coefficient observed during the passage of the main dust plume and E_{min} represents the background minimum observed prior to dust arrival. Higher values of I_{exco} indicate lower extinction relative to the maximum observed during the main dust plume and therefore represent a later/less strongly loaded stage of the observed dust event. This parameter is used only as an auxiliary component of the DAI and is not interpreted independently as a unique indicator of dust aging.Values calculated using Eq. (8) that approach 1 indicate a greater degree of dust aging, whereas values approaching 0 indicate relatively fresh dust with limited atmospheric processing.

$$I_{exco} = \frac{(E_{max} - E_{obs})}{(E_{max} - E_{min})} \tag{8}$$

The fluorescence sub-index (I_F) was constructed on the basis of stage-dependent variations in dust fluorescence spectra (see Fig. 4). During the passage of fresh dust, turbulent mixing with locally emitted organic materials and biomass-derived aerosols generates a pronounced fluorescence peak within the 445–465 nm wavelength range. As dust particles and their associated fluorescent constituents undergo atmospheric aging, the fluorescence spectrum progressively shifts towards longer wavelengths, reflecting changes in chemical composition and oxidation state. Therefore, the integrated fluorescence intensity within the 445–465 nm wavelength interval was selected as an indicator of relatively fresh dust, whereas the integrated fluorescence intensity within the 480–500 nm interval was used as an indicator of aged dust. Values calculated using Eq. (9) that approach 1 indicate a greater degree of dust aging, whereas values approaching 0 indicate relatively fresh dust with minimal atmospheric processing.

$$I_F = \frac{F_{(480-500)}}{F_{(445-465)} + F_{(480-500)}} \tag{9}$$

$$DAI = \frac{1}{3}(I_{VDR} + I_{exco} + I_F) \tag{10}$$

The three sub-indices were combined using equal weighting to obtain the Dust Aging Index (DAI), which is used here as an integrated optical indicator of the atmospheric processing state of dust-containing aerosol populations. Higher DAI values indicate optical characteristics more consistent with extensive atmospheric processing and aging-related evolution.

2.5. Correlation analysis between ionic composition and fluorescence spectra

To investigate the relationship between aerosol ionic composition and fluorescence spectral characteristics, the concentration of each measured ion was first normalized to the total concentration of all measured ions at each sampling time. The relative contribution of ion i was calculated as:

$$r_{i,t} = \frac{C_{i,t}}{\sum_{j=1}^{m} C_{j,t}} \tag{11}$$

where $C_{i,t}$ represents the concentration of ion i at time t, and m is the total number of measured ionic species. This normalization minimizes the influence of temporal variations in the overall ionic loading and emphasizes changes in relative ionic composition.

When repeated measurements were available within the same time point, the ion concentration fractions and fluorescence intensities were averaged within that time point to obtain the corresponding time series, $r_{i,t}$ and $S_{\lambda,t}$, respectively. Pearson's correlation coefficient was then calculated independently for each ion i and fluorescence wavelength λ:

$$\rho_{i,\lambda} = \frac{\sum_{t=1}^{N_t}(r_{i,t} - \bar{r}_i)(S_{\lambda,t} - \bar{S}_\lambda)}{\sqrt{\sum_{t=1}^{N_t}(r_{i,t} - \bar{r}_i)^2}\sqrt{\sum_{t=1}^{N_t}(S_{\lambda,t} - \bar{S}_\lambda)^2}} \tag{12}$$

here, N_t is the total number of time points, while $\bar{r}_i$ and $\bar{S}_\lambda$ represent the temporal means of the ion concentration fraction and fluorescence intensity at wavelength λ, respectively. Thus, $\rho_{i,\lambda}$ characterizes the temporal association between the relative contribution of ion i and the fluorescence intensity at wavelength λ. Positive and negative values indicate positive and negative associations, respectively.

2.6. Correlation analysis between particle size distribution and fluorescence spectra

To investigate the relationship between particle-size composition and fluorescence spectral characteristics, the particle size distribution and fluorescence spectrum were paired according to their common time bins. For each time bin t, the particle concentration in the k-th size interval was normalized by the total particle concentration across all size intervals:

$$p_{k,t} = \frac{C_{k,t}}{\sum_{j=1}^{n} C_{j,t}} \tag{13}$$

where $C_{k,t}$ is the particle concentration in the k-th size interval at time t, and n is the total number of size intervals. This normalization converts the particle concentration in each size interval into its relative contribution to the total particle population at each time bin.

The normalized particle fractions were then paired with the corresponding fluorescence intensities at each measured wavelength. For each of the three stages of the dust event, Pearson correlation coefficients were calculated between the time series of the particle fraction $p_{k,t}$ and the fluorescence intensity $S_{\lambda,t}$ at wavelength λ:

$$\rho_{k,\lambda} = \frac{\sum_{t=1}^{N_t}(p_{k,t} - \bar{p}_k)(S_{\lambda,t} - \bar{S}_\lambda)}{\sqrt{\sum_{t=1}^{N_t}(p_{k,t} - \bar{p}_k)^2}\sqrt{\sum_{t=1}^{N_t}(S_{\lambda,t} - \bar{S}_\lambda)^2}} \tag{14}$$

where N_t is the number of time bins within the corresponding stage, and $\bar{p}_k$ and $\bar{S}_\lambda$ are the temporal means of the particle fraction and fluorescence intensity, respectively. Thus, $\rho_{k,\lambda}$ quantifies the temporal correlation between the relative contribution of particles in the k-th size interval and the fluorescence intensity at wavelength λ. The correlation coefficients range from −1 to 1, with positive and negative values indicating synchronous and inverse temporal variations, respectively.

3. Results and discussion

3.1. Characteristics of aerosols above the observation site observed by lidar during the dust event

A severe dust pollution event was observed in Lanzhou from 25 to 26 March 2025. During the passage of the dust plume, the mass concentrations of PM_{10} and $PM_{2.5}$ exhibited substantial variability, and their temporal evolution showed a high degree of synchronization (Fig. 1). Particle concentrations increased sharply at approximately 23:00 on 25 March, indicating the arrival of the main dust plume over the

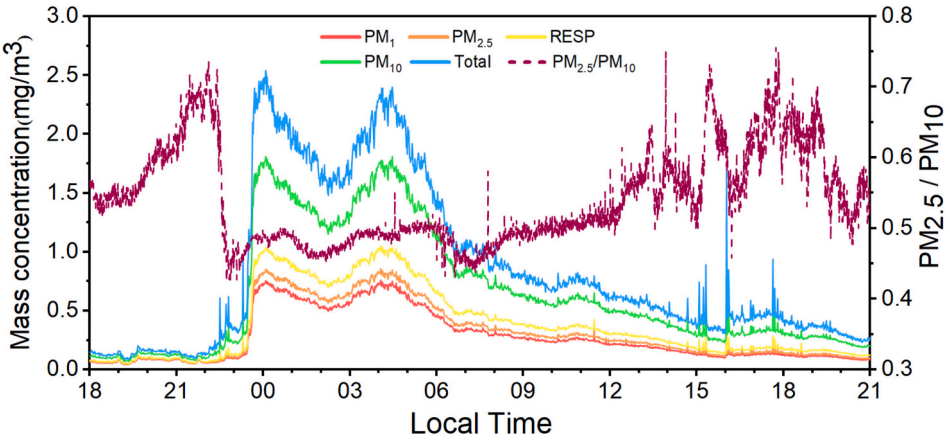

Fig. 1. Temporal variations in the mass concentrations of PM_1, $PM_{2.5}$, PM_{10}, respirable particulate matter (RESP), and the $PM_{2.5}/PM_{10}$ ratio during a severe dust event in Lanzhou from 18:00 LT on 25 March to 21:00 LT on 26 March 2025.

observation site (Zhang et al., 2022a). At approximately 03:00 on 26 March, particle concentrations exhibited a brief but pronounced decline, which was likely associated with transient meteorological variations such as increased wind speeds and shifts in wind direction that temporarily enhanced atmospheric dispersion conditions (Lu et al., 2019). Subsequently, particle concentrations increased rapidly once again and reached a second peak, which may have resulted either from a secondary intensification of the dust event or from the arrival of an additional dust-laden air mass (Yang et al., 2022; Zhang et al., 2025).

During the observation period, particle mass concentrations consistently followed the order PM_{10} > RESP (respirable particulate matter) > $PM_{2.5}$ > PM_1 (Fig. 1), indicating a pronounced dominance of coarse-mode particles, which is a characteristic feature of mineral dust aerosols and dust-dominated atmospheric conditions (Peng et al., 2019). The $PM_{2.5}/PM_{10}$ ratio is widely used as a diagnostic indicator for aerosol source identification and the assessment of aerosol mixing states (Zhang et al., 2025). Prior to the arrival of the main dust plume, the $PM_{2.5}/PM_{10}$ ratio gradually increased, likely because fine-particle-rich anthropogenic emissions near the surface were uplifted and redistributed by wind-induced turbulent mixing. At approximately 23:00 on 25 March, coincident with the arrival of the main dust plume, the $PM_{2.5}/PM_{10}$ ratio decreased rapidly, indicating a substantial increase in the contribution of freshly transported coarse dust particles. This observation further suggests that, during transport, the rapid changes observed in the dust-influenced aerosol layer may reflect external mixing with pre-existing/local pollution aerosols, atmospheric processing, or a combination of these processes. It should be noted that external mixing and atmospheric aging are not mutually exclusive processes. External mixing between dust and pollution aerosols can modify the observed optical and fluorescence properties and may precede or accompany subsequent chemical processing. Nevertheless, the substantial influx of coarse mineral dust particles increased the PM_{10} mass concentration disproportionately relative to $PM_{2.5}$, thereby reducing the $PM_{2.5}/PM_{10}$ ratio despite the occurrence of pollutant–dust mixing (Pan et al., 2017; Shin et al., 2015; Zhao et al., 2011).

Fig. 2 presents the lidar observations obtained during the dust event. Prior to the arrival of the main dust plume, fluorescence intensity, extinction coefficient, and volume depolarization ratio all remained at relatively low levels, indicating weak aerosol optical loading and limited aerosol optical influence within the atmospheric column. A low extinction coefficient generally reflects low aerosol loading, which is commonly associated with reduced particle mass and number concentrations. In contrast, a low volume depolarization ratio indicates a predominance of nearly spherical particles and a limited contribution from non-spherical components such as mineral dust, which typically generate elevated depolarization signals (Kong et al., 2022). Therefore,

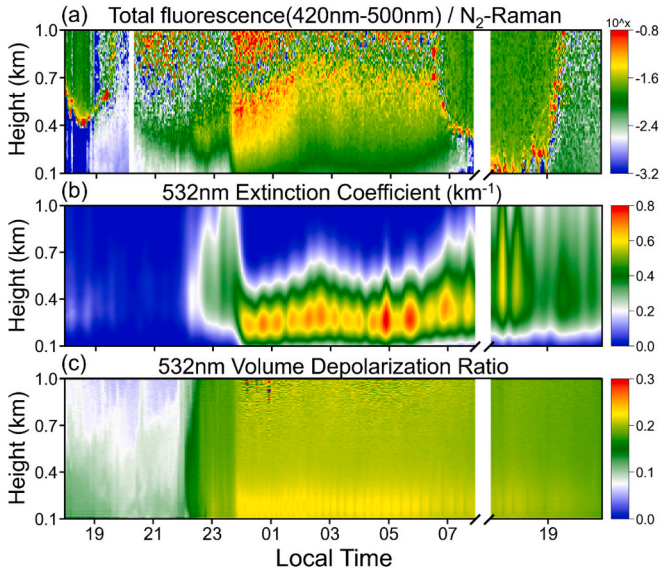

Fig. 2. Vertical distribution of atmospheric dust aerosols observed by the developed Mie scattering–polarization–fluorescence lidar from 18:00 LT on 25 March to 21:00 LT on 26 March 2025 during a severe dust event in Lanzhou. (a) Normalized total fluorescence intensity integrated over the wavelength range of 420–500 nm; (b) Aerosol extinction coefficient at 532 nm; and (c) Volume depolarization ratio at 532 nm.

the aerosol population during this stage was likely dominated by fine anthropogenic particulate matter, consistent with urban or regional pollution influences. Meanwhile, the fluorescence intensity exhibited a gradual increase throughout this period. Given that polluted aerosols are typically characterized by relatively high fluorescence intensities and low volume depolarization ratios, whereas dust is generally associated with weaker fluorescence signals and higher volume depolarization ratios, the pre-dust aerosol population was likely dominated by locally emitted anthropogenic pollutants, with a possible contribution from resuspended aged dust particles (Jiang et al., 2024; Tang et al., 2025).

During the passage of the main dust plume, the observation site entered a typical dust–pollution mixing stage characterized by simultaneously elevated fluorescence intensity, volume depolarization ratio, and extinction coefficient. The increase in the extinction coefficient reflects a rapid rise in aerosol loading, whereas the enhanced volume depolarization ratio indicates the dominance of non-spherical mineral dust particles within the aerosol population (Luo et al., 2015; Kong et al., 2022). Under externally mixed conditions, depolarization signals

originating from different aerosol components can be superimposed, thereby providing information on the extent of dust–pollution mixing within the atmosphere (Luo et al., 2015). The concurrent increase in fluorescence intensity is likely attributable to the adsorption or association of organic matter and fluorescent biological aerosols (e.g., pollen, bacteria, humic substances) with dust particles during long-range transport, with mineral dust serving as an effective carrier and transport medium (Wang et al., 2023a). In such dust–pollution mixed aerosols, both fluorescence intensity and volume depolarization ratio remain elevated, reflecting the combined optical signatures of fluorescent aerosol constituents and non-spherical mineral dust particles (Zhang et al., 2021a, 2021b; Chang et al., 2025). During daytime, enhanced photochemical activity driven by hydroxyl radicals promotes oxidation and nitration processes within mixed aerosols, leading to fluorescence quenching, progressive spectral redshifts, and changes in particle physicochemical properties. As the dust event evolves towards the dissipation stage, these aging processes are accompanied by decreases in fluorescence intensity, volume depolarization ratio, and extinction coefficient.

Overall, the simultaneous enhancement of fluorescence intensity, volume depolarization ratio, and extinction coefficient observed during the mixing stage provides strong evidence for extensive external mixing between mineral dust and fine anthropogenic particulate pollutants. This mixing process not only alters particle morphology but also modifies aerosol chemical composition, hygroscopic properties, and optical characteristics, thereby generating more complex vertical aerosol structures and potentially influencing atmospheric radiative forcing and climate-related processes (Chang et al., 2025).

To further investigate the evolution of the dust event, three representative periods were selected for detailed analysis: the initial stage (20:00 LT on 25 March), the dust–pollution mixing stage (04:00 LT on 26 March), and the dissipation stage (20:00 LT on 26 March). Based on lidar observations, vertical profiles of normalized fluorescence intensity (420–500 nm), volume depolarization ratio at 532 nm, and aerosol extinction coefficient at 532 nm were analyzed (Fig. 3). The fluorescence profiles indicate that, during the dust–pollution mixing stage, fluorescence intensity was generally higher than that observed during the initial and dissipation stages, particularly within the near-surface layer

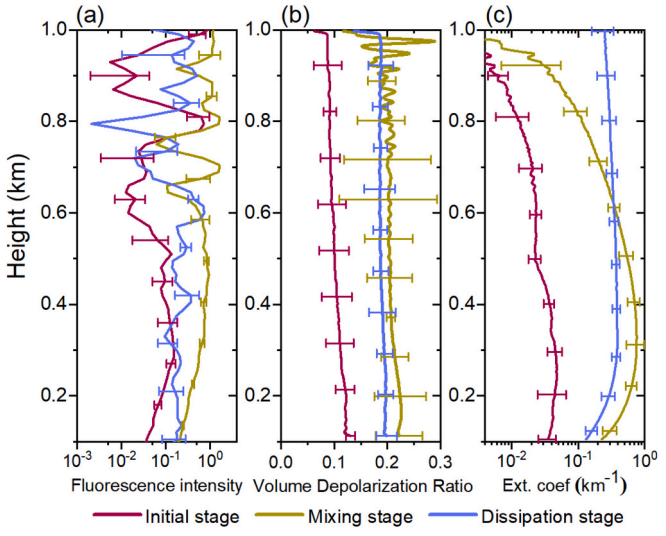

Fig. 3. Vertical profiles of (a) normalized total fluorescence intensity integrated over the wavelength range of 420–500 nm, (b) aerosol extinction coefficient at 532 nm, and (c) volume depolarization ratio at 532 nm observed by the lidar during three stages of dust evolution. The initial dust occurred at approximately 20:00 LT on 25 March, the dust–pollution mixing stage of dust was occurred at 04:00 LT on 26 March, and the dust dissipation stage occurred at 20:00 LT on 26 March.

below approximately 600 m, where the signal-to-noise ratio was relatively high. The maximum normalized fluorescence intensity reached 0.94. This observation suggests that mineral dust served as an effective carrier for organic pollutants and fluorescent biological aerosol components, thereby enhancing the observed fluorescence response through external mixing processes (Sugimoto et al., 2012a, 2012b; Jiang et al., 2024; Shang et al., 2026). Therefore, the enhanced fluorescence observed during this stage should not be interpreted as an exclusive signature of dust aging, because external mixing with fluorescent organic and biological aerosols may produce a similar optical response. The dissipation stage still exhibited higher fluorescence intensities than the initial stage, suggesting that residual externally mixed pollutants and aged aerosol components remained suspended within the atmosphere following the passage of the main dust plume (Jiang et al., 2024).

Meanwhile, both the volume depolarization ratio and the extinction coefficient reached their highest values during the dust–pollution mixing stage, with the extinction coefficient attaining 0.75 km^{-1} and the volume depolarization ratio reaching approximately 0.23. The elevated extinction coefficient reflects enhanced aerosol loading, whereas the increased volume depolarization ratio indicates a substantial contribution from non-spherical mineral dust particles within the aerosol population (Shang et al., 2026). In addition to providing information on particle morphology, the volume depolarization ratio can also provide insight into the aerosol mixing state. Under externally mixed conditions involving dust and anthropogenic aerosols, the volume depolarization ratio generally increases with the relative contribution of non-spherical particles. Furthermore, its combined variation with the extinction coefficient provides valuable constraints on aerosol loading, mixing characteristics, and particle composition (Luo et al., 2015).

3.2. *Differences in fluorescence spectra during different stages of dust evolution*

Based on observations from the fluorescence detection channels, distinct fluorescence spectral characteristics were identified during different stages of the dust event (Fig. 4). Prior to the arrival of the main dust plume, a pronounced fluorescence peak was observed within the 470–500 nm wavelength range. Compared with that observed during the dissipation stage, this fluorescence feature exhibited a longer peak wavelength and a broader spectral bandwidth, characteristics commonly associated with highly oxidized organic aerosols. Previous studies have demonstrated that, under 355 nm excitation, humic-like substances (HULIS) and partially oxidized secondary organic aerosols (SOA) typically emit fluorescence within the 420–500 nm wavelength range and exhibit progressive spectral redshifts and band broadening as their degree of oxidation increases (Li et al., 2019). Therefore, the long-wavelength fluorescence peak observed during this stage suggests the presence of aged organic matter and humic-rich aerosol components within the atmospheric column. Possible contributors include polycyclic aromatic hydrocarbons (PAHs) and their oxidation products associated with biomass burning, HULIS, and aged SOA, all of which exhibit fluorescence emissions within similar wavelength ranges under 355 nm excitation (Li et al., 2019). Consequently, the broad fluorescence feature within the 470–500 nm wavelength range is likely attributable to the combined contribution of highly oxidized HULIS and aged SOA. This observation further suggests that aged dust particles carrying oxidized organic components may have been transported into the overlying atmosphere prior to the arrival of the main dust plume through long-range atmospheric transport processes.

During the passage of fresh dust, intense turbulent mixing within the near-surface layer promoted interactions between dust particles and freshly emitted fluorescent materials, causing the fluorescence peak to shift towards shorter wavelengths and resulting in a distinct emission peak within the 445–465 nm wavelength range. This wavelength range is consistent with fluorescence emissions from several common aerosol constituents. For example, biological aerosols such as fungal spores and

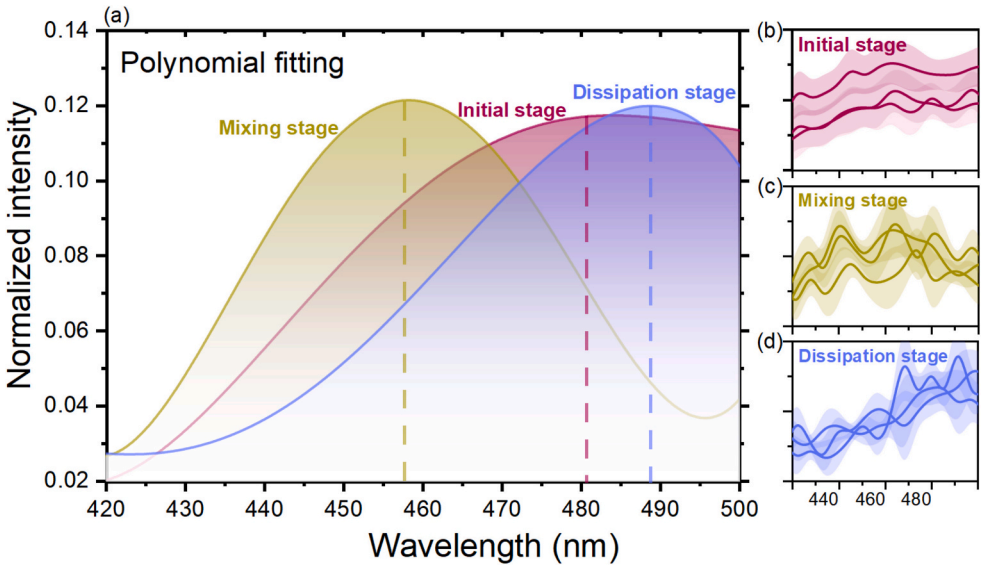

Fig. 4. Representative fluorescence spectra observed during the initial, dust–pollution mixing, and dissipation stages of the dust event. Panel (a) shows the polynomial-fitted fluorescence spectra, whereas panels (b–d) present the corresponding original fluorescence spectra.

bacteria typically emit at wavelengths below 480 nm under 355 nm excitation; freshly formed SOA commonly exhibit fluorescence peaks between approximately 464 and 475 nm; and certain protein-related compounds, including NAD(*P*)H-containing substances, emit within the 400–500 nm wavelength range (Zhang et al., 2021a, 2021b). Therefore, the fluorescence feature observed within the 445–465 nm wavelength range is likely associated with a mixed contribution from biological aerosols and freshly formed organic aerosol components. Previous studies have also demonstrated that mineral dust itself generally exhibits weak intrinsic fluorescence but can substantially enhance bulk fluorescence signals through the adsorption of fluorescent compounds onto particle surfaces (Huang et al., 2025a; Reichardt et al., 2025). This interpretation is consistent with the enhanced fluorescence observed during the dust–pollution mixing stage. Consequently, the observed short-wavelength shift and enhanced fluorescence intensity suggest that the aerosol population during this stage was dominated by externally mixed combinations of mineral dust and freshly emitted biological and organic aerosol components.

During the dissipation stage, the fluorescence peak gradually shifted back towards longer wavelengths. This fluorescence spectral redshift is consistent with the chemical processing and aging of organic components associated with the dust-containing aerosol population. As atmospheric oxidation processes driven by hydroxyl radicals and ozone proceed, organic aerosol constituents progressively develop more highly conjugated and chemically complex molecular structures. These transformations promote fluorescence emission at longer wavelengths and contribute to spectral broadening, both of which are characteristic features of aerosol aging (Afsana et al., 2023). In addition, the abundance of HULIS often increases during atmospheric aging, and their fluorescence emissions can extend to approximately 500 nm or even longer wavelengths (Sierra et al., 2005).

Meanwhile, during atmospheric transport, dust particles continuously interacted and mixed with regional pollution aerosols originating from biomass burning and industrial emissions. This process not only increased the fraction of organic aerosol but also promoted the formation of SOA and HULIS, thereby accelerating aerosol aging and enhancing the observed fluorescence redshift (Li et al., 2019). Therefore, the long-wavelength fluorescence shift observed during the dissipation stage likely reflects the combined effects of chemical transformation, oxidative processing, and progressive aging within externally mixed aerosol populations.

3.3. Evolution characteristics of the dust aging index above the observation site

Based on observations acquired using the Mie scattering–polarization–fluorescence lidar, significant variations in volume depolarization ratio, fluorescence spectral characteristics, and extinction coefficient were identified across different stages of the dust event. Previous studies have likewise demonstrated that these optical parameters are closely linked to dust aging processes, thereby providing a scientific basis for the quantitative assessment of dust aging using lidar-derived observations.

Because lidar signals below 600 m exhibited relatively high signal-to-noise ratios, this altitude range was selected to analyze the spatio-temporal evolution of the Dust Aging Index (DAI) (Fig. 5). Prior to the arrival of the main dust plume, relatively high DAI values were observed, with a maximum value (DAI_{max}) of 0.43. This phenomenon is likely associated with the wind-driven resuspension of previously deposited and chemically aged mineral dust particles. Following re-entrainment into the atmospheric boundary layer, these particles may have exhibited enhanced surface oxidation and accumulated pollutant coatings, thereby producing aerosols with more pronounced aging characteristics near the surface (Dentener et al., 1996; Finlayson-Pitts and Pitts, 2000; Reid et al., 2003; Usher et al., 2003). Previous studies have shown that resuspension processes can enhance particle internal mixing, hygroscopicity, and the accumulation of secondary inorganic salts and organic matter on particle surfaces, thereby promoting the development of aerosol aging characteristics (Kok, 2011b; Reid et al., 2003; Shao et al., 2011).

As the fresh dust plume passed over the observation site, the DAI decreased rapidly, reaching a minimum value (DAI_{min}) of 0.32, indicating the dominance of newly transported mineral dust particles. Such particles typically originate from arid and semi-arid source regions and are composed predominantly of quartz, feldspar, and clay minerals. They generally exhibit irregular morphologies and limited surface coatings of secondary inorganic and organic materials, resulting in relatively weak atmospheric processing and low degrees of chemical aging (Chin and Kahn, 2009; Mahowald et al., 2008). Both observational and modelling studies have demonstrated that fresh dust generally exhibits lower hygroscopicity, weaker light-absorption enhancement, and reduced chemical transformation compared with aged dust particles (Chin and Kahn, 2009; Choobari et al., 2014).

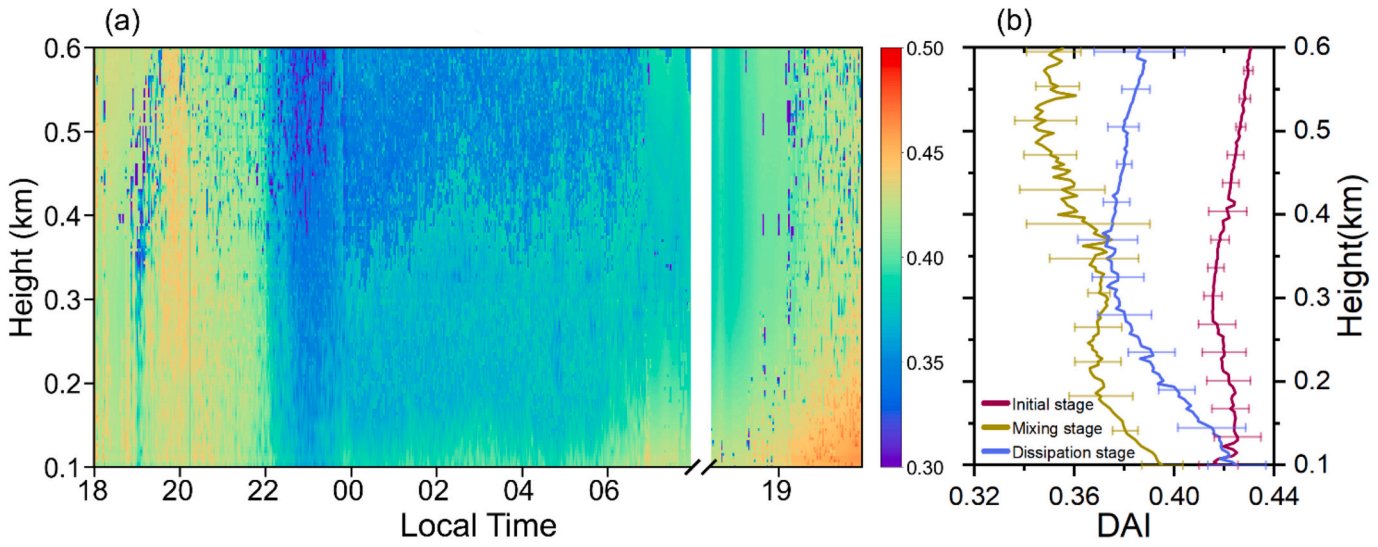

Fig. 5. (a) Spatiotemporal evolution of the DAI below 600 m, derived from observations acquired by the Mie scattering–polarization–fluorescence lidar during the dust event in Lanzhou from 18:00 LT on 25 March to 21:00 LT on 26 March 2025; and (b) vertical DAI profiles during the initial, dust–pollution mixing, and dissipation stages of the dust event.

During subsequent atmospheric transport and mixing, dust particles continuously underwent oxidation by hydroxyl (OH) and nitrate (NO_3) radicals while simultaneously experiencing photochemical aging and interactions with regionally polluted air masses. These processes promoted the gradual accumulation of sulfate, nitrate, and secondary organic aerosol (SOA) species on particle surfaces (Dentener et al., 1996; Usher et al., 2003; Seinfeld and Pandis, 2016). These processes enhanced particle hygroscopicity, altered particle refractive indices, and promoted the transformation of aerosol populations from predominantly externally mixed to more internally mixed states, thereby significantly modifying their optical properties (Dentener et al., 1996; Finlayson-Pitts and Pitts, 2000; Jimenez et al., 2009). Consequently, the DAI gradually increased and reached approximately 0.42 during the dissipation stage, reflecting the progressive aging and chemical transformation of the dust–pollution aerosol mixture. This characteristic "decreasing–increasing" non-monotonic pattern highlights the strong temporal evolution of the dust aging process, reflecting the transition from aged background aerosols to freshly transported dust and subsequently to chemically processed mixed aerosols (Müller et al., 2007).

Vertically, DAI values were generally higher near the surface than at higher altitudes, reflecting a characteristic vertically stratified aging structure within the atmospheric column. Near-surface aerosols are more strongly influenced by anthropogenic emissions, dust-resuspension processes, and repeated deposition– –re-entrainment cycles, resulting in enhanced accumulation of secondary inorganic salts, organic coatings, and biological aerosol components on particle surfaces (Jeffrey et al., 2003; Mao et al., 2026). In contrast, dust layers at higher altitudes more commonly represent recently transported air masses that retain stronger mineralogical characteristics, lower degrees of chemical oxidation, and less extensive atmospheric processing, thereby resulting in lower DAI values (Graber and Rudich, 2006; Chin and Kahn, 2009; Choobari et al., 2014; Mao et al., 2026).

3.4. Validation of the DAI using the concentration ratio of nitrate to calcium ions

To validate the Dust Aging Index (DAI), the concentration ratio of nitrate (NO_3^-) to calcium (Ca^{2+}) was employed, as this parameter is widely recognized as a robust indicator of mineral dust aging. The ratio reflects the extent of heterogeneous reactions between carbonate minerals (e.g., $CaCO_3$) present in dust particles and acidic gases, primarily HNO_3, resulting in the formation of calcium nitrate ($Ca(NO_3)_2$). Therefore, the NO_3^-/Ca^{2+} ratio effectively reflects the progression of mineral dust from a relatively fresh state to a chemically aged state and has been widely used as an indicator of dust aging in both field observations and laboratory studies (Usher et al., 2003; Goel et al., 2020; Zhang et al., 2022b; Li et al., 2023a, 2023b; Li et al., 2025).

To facilitate comparison of the temporal evolution of the DAI and the NO_3^-/Ca^{2+} ratio, Min–Max normalization was applied to both variables, linearly scaling them to the interval [0,1]. This procedure removes dimensional differences and highlights temporal variation patterns rather than absolute magnitudes (Dai et al., 2024). Pearson correlation coefficients (r) and the corresponding *p*-values were subsequently calculated to evaluate the strength and statistical significance of the linear relationship between the normalized DAI and the normalized NO_3^-/Ca^{2+} ratio.

The correlation analysis results (Fig. 6) demonstrate that the lidar-derived DAI exhibits a high degree of consistency with the normalized NO_3^-/Ca^{2+} ratio throughout the dust event. This strong agreement can be explained by two primary mechanisms. First, nitrate coatings formed during dust aging alter particle morphology and surface properties, thereby reducing volume depolarization ratios and modifying aerosol scattering characteristics (Zhang et al., 2022a, 2022b). Second, the formation of nitrate salts and the associated enhancement of particle hygroscopicity modify aerosol size distributions, refractive indices, and optical responses, thereby producing detectable variations in lidar signals (Zhang et al., 2022a; Li et al., 2025). Therefore, the chemical aging represented by the NO_3^-/Ca^{2+} ratio is fundamentally consistent with the evolution of aerosol optical properties observed by lidar, providing a strong physical basis for the use of the DAI as an indicator of dust aging.

These results further demonstrate the reliability of the multi-parameter lidar-derived DAI for characterizing dust chemical evolution and provide a robust foundation for the quantitative remote sensing of dust-aging processes.

3.5. Variations in water-soluble ion and gaseous pollutant concentrations during the dust event

Fig. 7 presents the temporal variations in major water-soluble ions and gaseous pollutants during the severe dust event. As a widely recognized tracer of mineral dust, Ca^{2+} concentrations increased rapidly during the passage of the dust plume and subsequently decreased gradually as dust particles settled from the atmosphere (Usher et al., 2003; Li et al., 2025). Similar temporal variations were observed for

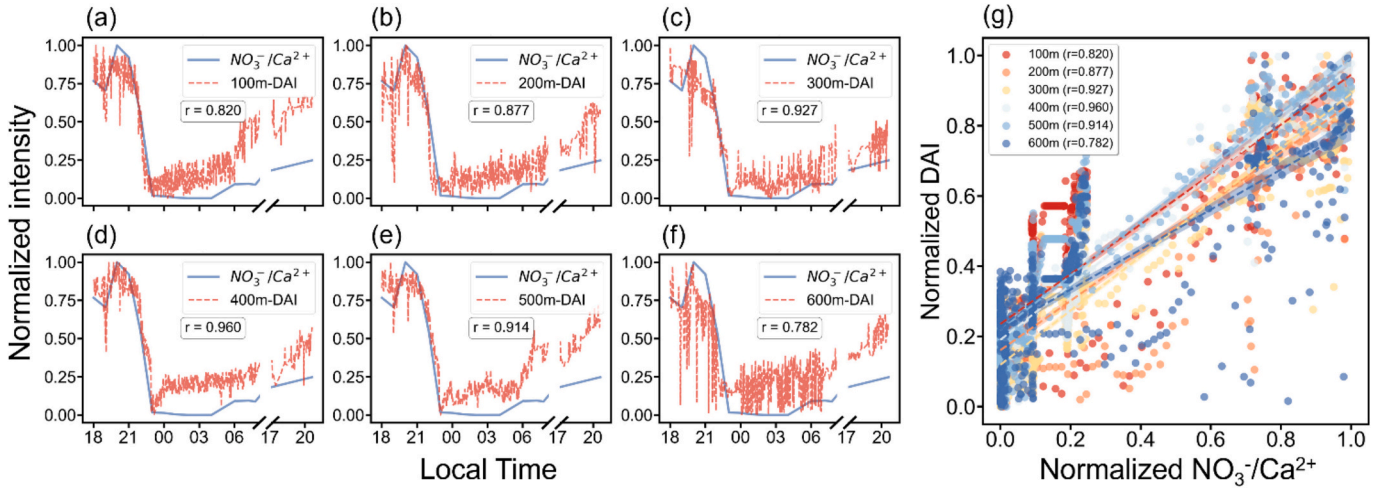

Fig. 6. Validation of the DAI using the nitrate-to-calcium ion concentration ratio (NO_3^-/Ca^{2+}). (a–f) Comparison between the normalized DAI and the normalized NO_3^-/Ca^{2+} concentration ratio at different altitudes; and (g) correlation analysis between the normalized DAI and the normalized NO_3^-/Ca^{2+} concentration ratio based on DAI time series at 100, 200, 300, 400, 500, and 600 m, together with the corresponding statistical significance tests.

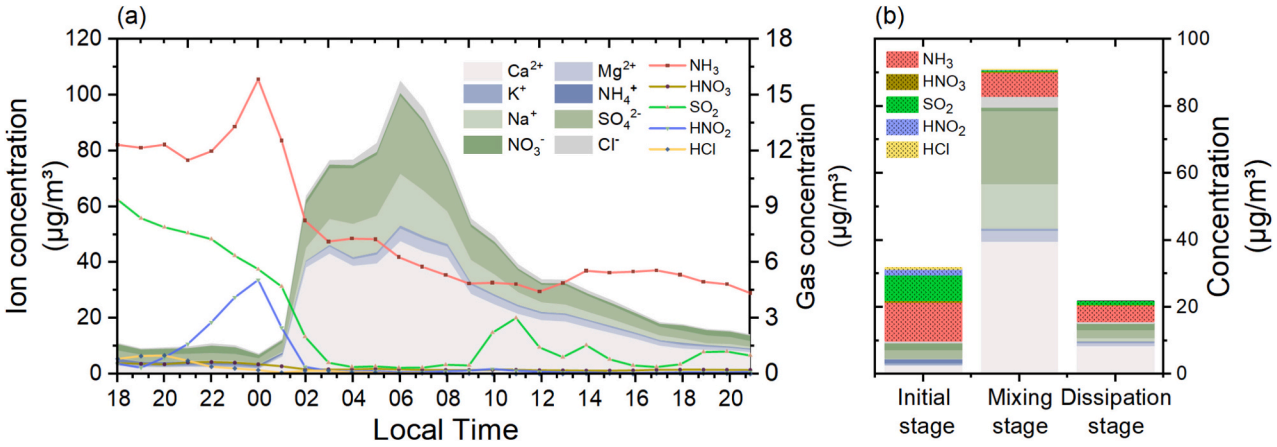

Fig. 7. Temporal variations and stage-dependent characteristics of water-soluble ions and gaseous pollutants during the dust event in Lanzhou from 18:00 LT on 25 March to 21:00 LT on 26 March 2025. (a) Temporal variations in the concentrations of water-soluble ions and gaseous pollutants. (b) Relative concentration ratios of water-soluble ions and gaseous pollutants during the initial, dust–pollution mixing, and dissipation stages of the dust event.

the crustal-derived ions Mg^{2+} and K^+, further confirming the dominant contribution of mineral dust to the observed aerosol composition (Usher et al., 2003; Chen et al., 2011). In addition to increasing particulate mass concentrations, mineral dust actively participates in heterogeneous reactions with acidic trace gases, promoting the formation of nitrate- and sulfate-containing secondary species and thereby modifying atmospheric chemical composition (Usher et al., 2003; Bones et al., 2010; Chen et al., 2011).

Across the initial, dust–pollution mixing, and dissipation stages, SO_2, HNO_3, and NH_3 exhibited an overall increasing–decreasing–increasing trend, reflecting the combined influences of atmospheric transport, dilution processes, and gas–particle partitioning (Ervens et al., 2011; Guo et al., 2016). Sulfuric acid produced through the atmospheric oxidation of SO_2 possesses extremely low volatility and promotes particle growth through condensation processes. It also provides favorable surfaces for the uptake and condensation of organic vapors, thereby facilitating the formation of secondary organic aerosol (SOA) (Carlton et al., 2007; Ervens et al., 2011). Meanwhile, NH_3 neutralizes H_2SO_4 and HNO_3 to form ammonium salts, thereby enhancing aerosol hygroscopicity and increasing aerosol liquid water content (ALWC). The resulting increase in particle-phase water facilitates multiphase oxidation processes and oligomerization reactions, which contribute to the formation and aging of secondary aerosols (Ervens et al., 2011; Guo et al., 2016; Pye et al., 2020). In addition, NH_3 may participate in atmospheric organic reactions that produce nitrogen-containing organic compounds (NOCs), which can contribute to SOA formation and increase the chemical complexity of aged aerosol particles (Lim et al., 2010; Ervens et al., 2011).

Night-time SOA formation is primarily driven by NO_3 radicals and N_2O_5-mediated chemistry rather than by HNO_3 directly. NO_3 radicals oxidize volatile organic compounds (VOCs), leading to the formation of organic nitrates and other low-volatility oxidation products that represent an important source of night-time SOA (Brown and Stutz, 2012; Ng et al., 2017). Simultaneously, the hydrolysis of N_2O_5 within aerosol liquid water produces HNO_3, which subsequently promotes the formation of particulate inorganic nitrate through gas–particle partitioning and heterogeneous chemical processes (Chen et al., 2011; Ng et al., 2017). Following the arrival of the dust plume, HONO and HCl concentrations decreased continuously, likely as a result of uptake by mineral dust particles, heterogeneous chemical reactions on particle surfaces, and boundary-layer mixing processes that modified the distribution of reactive trace gases (Usher et al., 2003; Chen et al., 2011).

The concentrations of NH_4^+ and NO_3^- exhibited an overall increasing–decreasing–increasing trend during the dust event, whereas SO_4^{2-}

and Cl^- showed contrasting temporal variations, reflecting differences in their emission sources, chemical formation pathways, and atmospheric processing mechanisms (Guo et al., 2016; Pye et al., 2020). Together, NH_4^+, NO_3^-, and SO_4^{2-} are major contributors to ALWC, which provides a critical medium for multiphase chemical reactions and secondary aerosol formation (Ervens et al., 2011; Guo et al., 2016). Under such conditions, water-soluble organic precursors, including glyoxal, methylglyoxal, and related carbonyl compounds, can undergo aqueous-phase oxidation and oligomerization reactions, leading to the formation of aqueous-phase SOA (aqSOA) (Lim et al., 2010; Ervens et al., 2011). Moreover, aged mineral dust, particularly particles coated with nitrate and other secondary species, exhibits enhanced hygroscopicity and can serve as an efficient medium for liquid-phase chemical reactions, thereby further promoting SOA formation and aerosol aging (Cwiertny et al., 2008; Li et al., 2025). The ionic balance, particularly the neutralization of SO_4^{2-} and NO_3^- by NH_4^+, strongly influences aerosol acidity (pH), which in turn regulates multiphase reaction pathways, including acid-catalyzed reactions, organosulfate formation, and other aqueous-phase transformation processes (Guo et al., 2016; Pye et al., 2020). Aerosol pH may also influence SOA formation by modulating the production and reactivity of reactive oxygen species (ROS), thereby affecting oxidation pathways and the chemical evolution of secondary aerosols (Tong et al., 2018).

Previous studies have demonstrated that aerosol fluorescence primarily originates from organic compounds containing conjugated chromophoric structures, including aromatic compounds, humic-like substances (HULIS), and proteinaceous materials. Furthermore, fluorescence emissions progressively shift towards longer wavelengths as molecular conjugation and the degree of oxidation increase (Coble, 1996; Pan, 2015; Laskin et al., 2015). To further investigate the relationship between aerosol chemical evolution and optical-property signal variations during the dust event, correlation analyzes were conducted between fluorescence spectral characteristics and ion chromatographic measurements.

During the initial stage (Fig. 8a), fluorescence within the 430–450 nm wavelength range exhibited strong positive correlations with Cl^-, NO_3^-, NH_4^+, NH_3, suggesting that the aerosol population was strongly influenced by secondary inorganic salts and freshly formed SOA. During this stage, NH_3 promoted gas–particle partitioning and facilitated the formation of nitrogen-containing organic compounds and weakly absorbing brown carbon (BrC), thereby contributing to the chemical evolution of secondary aerosols (Pinder et al., 2007; Farmer and Jimenez, 2010; Seinfeld and Pandis, 2016). Because these organic compounds generally possess relatively low molecular weights and less extensively conjugated chromophoric structures, their fluorescence emissions are typically concentrated within the 400–450 nm wavelength range (Jimenez et al., 2009; Laskin et al., 2015). In addition, the observed correlations between Ca^{2+} and long-wavelength fluorescence suggest that mineral dust acted as a medium for heterogeneous chemical reactions, promoting the enrichment of organic matter and the formation of HULIS, rather than contributing directly to fluorescence through the inorganic mineral components themselves (Usher et al., 2003; Graber and Rudich, 2006).

During the dust–pollution mixing stage (Fig. 8b), enhanced mineral dust loading provided abundant reactive surfaces that promoted the heterogeneous processing of SO_2 and NOx, thereby facilitating the formation of internally and externally mixed organic–inorganic aerosol populations (Dentener et al., 1996; Finlayson-Pitts and Pitts, 2000; Wang et al., 2018a). Simultaneously, oxidation products derived from volatile organic compounds (VOCs) underwent further oligomerization and polymerization, reactions, leading to increased molecular conjugation and chemical complexity. These transformations contributed to spectral broadening and a progressive shift of fluorescence emissions towards longer wavelengths. The observed correlations among HNO_3, HONO, and SO_2 suggest that this stage represented a transitional chemical regime in which secondary aerosol formation and aerosol aging occurred concurrently (Bones et al., 2010; Ng et al., 2010; Laskin et al., 2015).

During the dissipation stage (Fig. 8c), the contribution of coarse particles gradually decreased, and the aerosol population became increasingly influenced by highly oxidized organic aerosols (OOA) and HULIS. The presence of these highly oxidized organic species, characterized by greater molecular complexity and more extensively conjugated chromophoric structures, contributed to a shift in fluorescence emissions towards wavelengths above 450 nm (Coble, 1996; Jimenez et al., 2009; Ng et al., 2010). At the same time, the continued involvement of NH_3, HNO_3, and HCl in gas–particle partitioning and heterogeneous chemical processes promoted the formation of nitrogen-containing organic compounds and BrC (Pinder et al., 2007; Seinfeld and Pandis, 2016). In addition, transition-metal components within mineral dust may enhance the generation of reactive oxygen species (ROS) through photochemical and Fenton-like reactions, thereby accelerating the oxidation, functionalization, and oligomerization of organic compounds (Deguillaume et al., 2005; George et al., 2015).

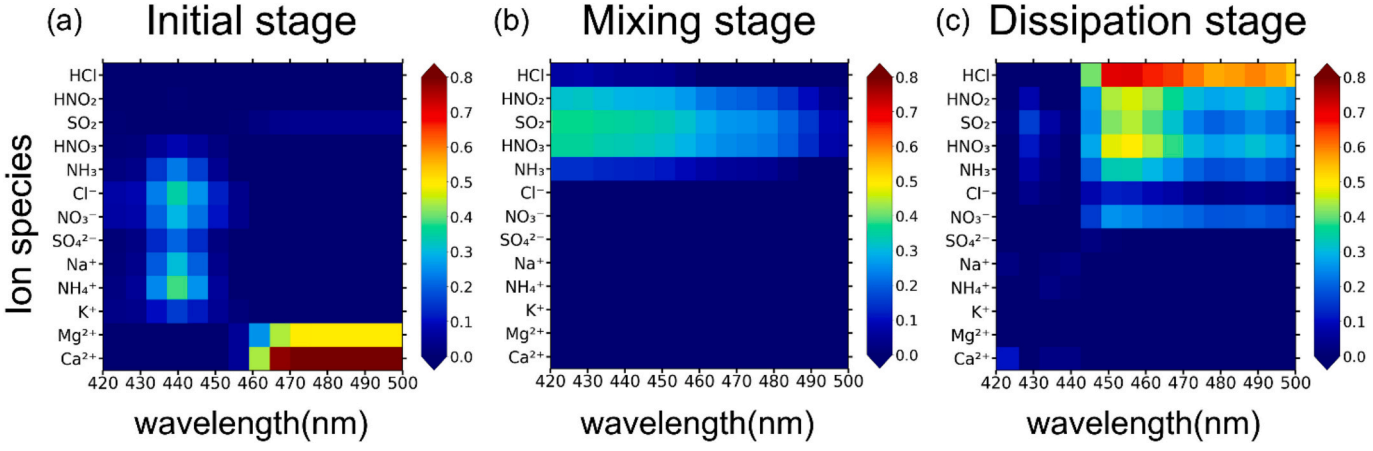

Fig. 8. Pearson correlation coefficients between fluorescence spectra (420–500 nm) and water-soluble ions and gaseous pollutants for the three stages of the dust event: (a) initial stage, (b) mixing stage, and (c) dissipation stage. For each stage, the temporal series of the concentration fraction of each ion species was correlated independently with the fluorescence intensity at each wavelength using matched time bins. The horizontal axis denotes fluorescence wavelength (nm), the vertical axis denotes ion species, and the color represents the dimensionless Pearson correlation coefficient (ρ).

3.6. Variation characteristics of the submicron (9–371 nm) particle size distribution during the dust event

The particle size distribution analyzed in this study covered the diameter range of 9–371 nm and primarily reflected variations in the number concentrations of submicron aerosol particles (Fig. 9) (Coquelin et al., 2013; Wu and Boor, 2021). During the initial stage of the dust event, the particle size distribution was dominated by particles with diameters smaller than 200 nm. This feature may be attributed to the upward transport of near-surface pollutants by enhanced wind fields, together with the mechanical fragmentation of mineral dust particles during transport and particle–particle collisions, which can generate substantial numbers of submicron particles (Kok, 2011a, 2011b). Previous studies have also shown that fine particles during dust events can transport substantial quantities of biological aerosol components, including bacteria, fungal spores, and biological fragments (Polymenakou et al., 2008). These biological materials are frequently associated with submicron particles, which exhibit strong long-range transport capability and enhanced respiratory deposition efficiency within the human respiratory tract. Moreover, particles within the 70–200 nm size range are often strongly influenced by secondary aerosol formation processes, particularly the formation of secondary organic aerosol (SOA) through the condensation of oxidation products derived from volatile organic compounds (VOCs) (Wu and Boor, 2021; Chen et al., 2022). Because submicron particles can efficiently penetrate the alveolar region of the lungs, they may pose significant risks to health, particularly through enhanced respiratory exposure and deposition (Rückerl et al., 2011).

As the dust event entered the dust–pollution mixing stage, the number concentration of particles with diameters exceeding 200 nm increased substantially and gradually became the dominant contributor to the total aerosol number concentration. This shift was closely associated with the influx of regionally transported mineral dust, which typically contributes substantially to aerosol mass within the 0.5–10 μm particle-size range (Avino and Manigrasso, 2017). In addition, airborne microorganisms, including bacteria and fungi, are commonly associated with inhalable particles within the approximate size range of 1–5 μm. Within this size range, coarse particles are more likely to transport intact microbial cells, whereas smaller particles predominantly contain microbial fragments, metabolites, or cellular debris (Rückerl et al., 2011). For example, soil-derived microorganisms such as *Bacillus* spp. are frequently detected in particles larger than 3.3 μm during dust events, whereas smaller particles are often enriched in actinomycetes and other environmentally derived microbial communities (Polymenakou et al., 2008). These findings suggest that dust transport acts not only as an efficient pathway for the dispersion of mineral particles but also as an important mechanism for the long-range transport of microorganisms, microbial fragments, and biologically derived organic matter.

During the dissipation stage, gravitational settling progressively removed coarse particles from the atmosphere, causing the particle size distribution to shift back towards fine particles with diameters smaller than 200 nm. Aerosols during this stage were likely dominated by hydrocarbon-like organic aerosols (HOA) associated with primary emissions, together with secondary organic aerosols (SOA) and secondary inorganic salts formed through gas–particle partitioning processes, including sulfate, nitrate, and ammonium species (Wu and Boor, 2021; Chen et al., 2022). These fine particles can further serve as condensation sites for oxidation products derived from biogenic volatile organic compounds (BVOCs), thereby promoting particle growth and potentially contributing to new particle formation processes (Chen et al., 2022). In addition, metal oxides commonly present in mineral dust, such as Fe_2O_3 and TiO_2, can exhibit photocatalytic activity under solar radiation, thereby enhancing the oxidation of organic compounds and accelerating both SOA formation and aerosol aging processes. This process is considered an important mechanism linking dust–pollutant interactions, secondary aerosol formation, and the chemical evolution of atmospheric aerosols (Aiyuk et al., 2024).

The relationship between particle size distributions and fluorescence spectral characteristics further reflects variations in aerosol chemical composition and aging state across different particle-size ranges. In general, submicron particles, particularly those smaller than 200 nm, are more closely associated with recently formed particles and relatively fresh SOA, whereas larger particles (>300 nm) are more strongly influenced by condensational growth, coagulation processes, and contributions from mineral dust and aged aerosol components (Jimenez et al., 2009; Seinfeld and Pandis, 2016). Therefore, correlation analyzes between particle size distributions and fluorescence spectral characteristics (Fig. 10) provide additional insight into the links among aerosol chemical evolution, particle growth processes, and changes in aerosol optical properties during the dust event.

During the initial stage of the dust event (Fig. 10a), fluorescence within the 420–450 nm wavelength range exhibited strong correlations with particles in the 70–130 nm size range, suggesting that these particles were strongly influenced by newly formed SOA and relatively weakly oxidized organic matter produced through nucleation and condensational growth following the oxidation of volatile organic

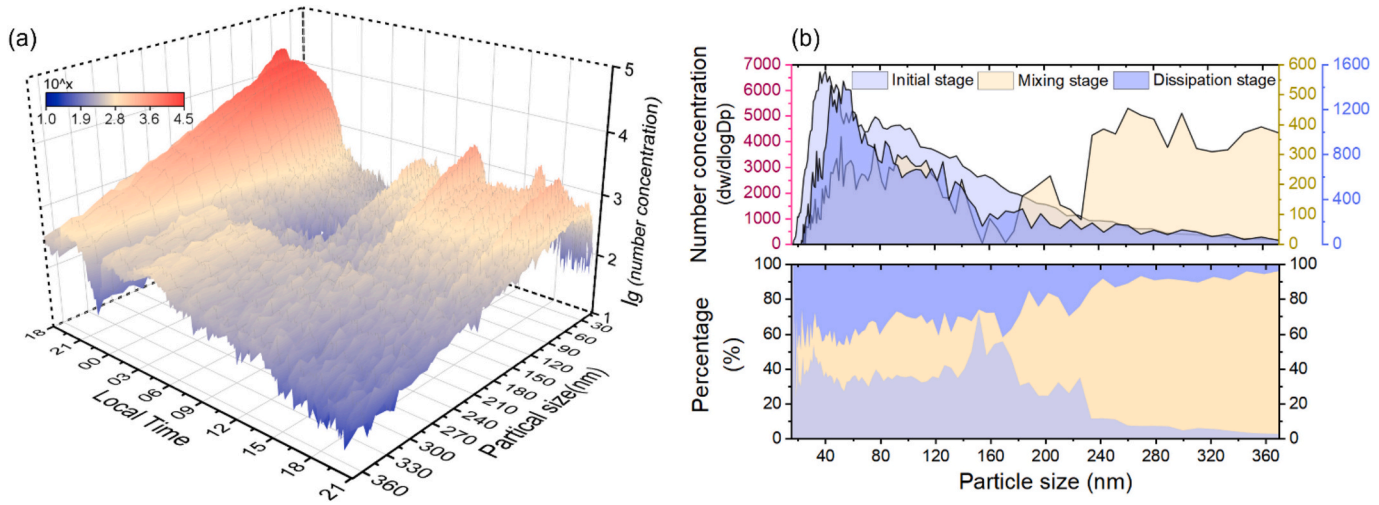

Fig. 9. Temporal variations and particle size-distribution characteristics of atmospheric aerosols during the dust event in Lanzhou from 18:00 LT on 25 March to 21:00 LT on 26 March 2025. (a) Temporal variations in the number concentration of particles within the 9–371 nm size range; and (b) particle size distributions during the initial, dust–pollution mixing, and dissipation stages of the dust event.

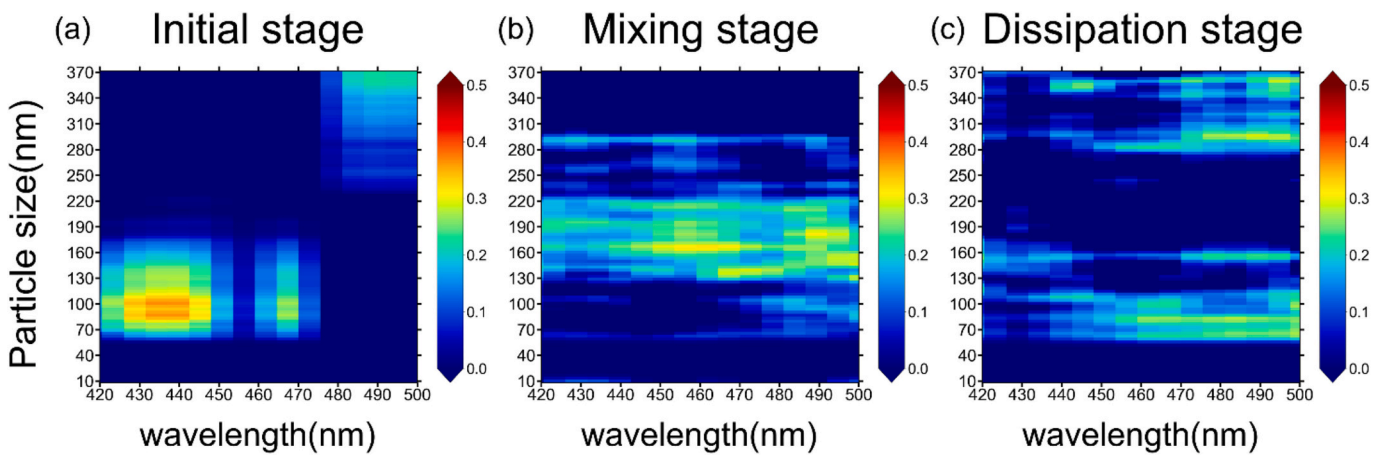

Fig. 10. Pearson correlation coefficients between fluorescence spectral characteristics (420–500 nm) and particle size distributions (9–371 nm) during the three stages of the dust event: (a) initial stage, (b) mixing stage, and (c) dissipation stage. For each particle-size bin, its temporal variation in relative contribution to the total particle concentration was correlated independently with the fluorescence intensity at each wavelength using matched time bins. The horizontal axis represents fluorescence wavelength, the vertical axis represents particle-size bins, and the color indicates the dimensionless Pearson correlation coefficient (ρ).

compounds (VOCs) (Zhang et al., 2007; Jimenez et al., 2009). In contrast, fluorescence emissions at wavelengths above 480 nm were more strongly associated with particles larger than 310 nm, suggesting that these larger particles had undergone more extensive atmospheric processing and were enriched with humic-like substances (HULIS) and partially oxidized organic matter (Usher et al., 2003; Graber and Rudich, 2006).

During the dust–pollution mixing stage (Fig. 10b), correlations between particles within the 130–220 nm size range and fluorescence emissions across the 420–500 nm wavelength range became substantially stronger. This pattern suggests continuous particle growth through condensational and coagulation processes, accompanied by progressive oxidation, functionalization, and polymerization of organic compounds. As molecular conjugation and chemical complexity increased, fluorescence emissions broadened and progressively shifted towards longer wavelengths, reflecting the formation of more highly oxidized and structurally complex organic aerosol components (Zhang et al., 2007; Jimenez et al., 2009; Ng et al., 2010).

During the dissipation stage (Fig. 10c), particles within the 50–110 nm size range again exhibited strong correlations with fluorescence emissions at wavelengths above 460 nm, suggesting that highly oxidized and low-volatility compounds, including oxidation products derived from biogenic volatile organic compounds (BVOCs) and regionally transported pollutants, contributed to particle growth and potentially to new particle formation processes (Zhang et al., 2007; Ng et al., 2010). Meanwhile, correlations between particles larger than 280 nm and fluorescence emissions above 470 nm suggest continued aerosol aging and atmospheric processing, with particle surfaces becoming increasingly enriched in high-molecular-weight organic compounds and HULIS (Coble, 1996; Graber and Rudich, 2006).

Overall, the coupled evolution of fluorescence spectral characteristics, chemical composition, and particle size distributions reveals the continuous aging process of dust aerosols from the initial stage through the dust–pollution mixing stage to the subsequent advanced aging stage. During the initial stage, aerosols were predominantly influenced by freshly formed SOA and secondary inorganic salts. Their relatively low degree of oxidation and limited molecular conjugation resulted in fluorescence emissions being concentrated within the short-wavelength region (approximately 400–450 nm). At the same time, the observed correlations between fine particles and ions such as NH_4^+ and NO_3^- suggest substantial contributions from gas–particle partitioning processes and the formation of newly generated organic matter (Jimenez et al., 2009; Seinfeld and Pandis, 2016).

As the dust entered the dust–pollution mixing stage, mineral particles provided abundant reactive surfaces that enhanced heterogeneous reactions involving SO_2, NOx, and VOCs, thereby promoting the formation of nitrogen-containing organic compounds and brown carbon (BrC) (Ng et al., 2010; Laskin et al., 2015; Seinfeld and Pandis, 2016). Simultaneously, increases in particle size and the accumulation of secondary inorganic ions suggest continuous oxidation, functionalization, and molecular complexation of organic aerosol constituents, leading to fluorescence spectral broadening and progressive redshifts towards longer wavelengths.

During the dissipation stage, aerosols became increasingly influenced by highly oxidized organic aerosols (OOA) and HULIS. The greater molecular complexity and more extensively conjugated chromophoric structures of these aged organic components contributed to fluorescence emissions becoming increasingly concentrated at wavelengths above 450 nm. In addition, the observed correlations between larger particles and long-wavelength fluorescence suggest substantial organic coating formation and enrichment of humic-like substances on dust-associated particle surfaces (Usher et al., 2003; Jimenez et al., 2009; Ng et al., 2010; Laskin et al., 2015).

Overall, the combined evolution of particle size distributions and ionic composition demonstrates the progressive transformation of organic aerosols from relatively low-molecular-weight SOA species to highly oxidized compounds with extensively conjugated structures, including HULIS and BrC. The progressive fluorescence redshift from shorter to longer wavelengths represents a direct optical manifestation of this chemical aging process, reflecting increasing molecular conjugation, oxidation, and chemical complexity within the organic aerosol fraction (Jimenez et al., 2009; Bones et al., 2010; Ng et al., 2010).

4. Conclusions

This study combined multi-parameter lidar observations with in situ measurements to systematically investigate the aging processes of dust aerosols during a severe dust event. Based on the coupled evolution of aerosol optical, microphysical, and chemical properties, a novel Dust Aging Index (DAI) was developed to quantitatively characterize the mixing process and aging state of dust aerosols.

(1) A robust optical index for dust aging was established. By integrating the volume depolarization ratio, extinction coefficient, and fluorescence spectral characteristics, the DAI effectively captures both the physical evolution of dust aerosols, including changes in particle morphology and aerosol mixing state, and their chemical evolution associated with organic oxidation,

heterogeneous processing, and secondary aerosol formation. Compared with conventional single-parameter indicators, the DAI provides a more continuous and comprehensive framework for quantifying dust-minxing-aging processes.

(2) The DAI exhibited a distinct non-monotonic temporal evolution pattern during the dust event. Elevated DAI values were observed prior to the arrival of the main dust plume, likely associated with the resuspension of previously deposited and chemically aged particles within the near-surface atmosphere. As freshly transported mineral dust became dominant, the DAI decreased rapidly, reflecting the increased contribution of relatively fresh, externally mixed, and weakly processed particles. During the subsequent transport and dissipation stages, the DAI gradually increased again as heterogeneous reactions, secondary aerosol formation, and aerosol aging processes became increasingly important. This characteristic "decrease–increase" pattern highlights the dynamic interplay between fresh dust input and atmospheric chemical aging.

(3) Fluorescence spectral redshift provided a useful optical signature consistent with the atmospheric processing and aging-related evolution of fluorescent organic components associated with dust-containing aerosols. During the aging process, fluorescence emission peaks gradually shifted from shorter wavelengths (445–465 nm) towards longer wavelengths (480–500 nm), accompanied by progressive spectral broadening. This spectral evolution was closely associated with increasing oxidation levels, enhanced molecular conjugation, and the accumulation of humic-like substances (HULIS) and other highly oxidized organic compounds. The observed fluorescence redshift therefore provides direct optical evidence of the chemical transformation and aging of dust-associated organic matter during atmospheric transport.

(4) Strong coupling relationships among aerosol chemical composition, particle size distributions, and optical properties were observed. Long-wavelength fluorescence exhibited significant correlations with submicron particles and secondary inorganic ions, suggesting that heterogeneous reactions and secondary aerosol formation play critical roles in dust aging. In particular, the strong consistency between the temporal evolution of the DAI and the NO_3^-/Ca^{2+} ratio further demonstrates that the optical evolution detected by lidar is intrinsically linked to the chemical aging processes of mineral dust.

Overall, this study demonstrates that scattering–polarization–fluorescence lidar provides an effective approach for real-time and vertically resolved monitoring of dust-aging processes. The proposed DAI establishes a quantitative link between aerosol optical evolution and chemical transformation, thereby providing a novel remote-sensing framework for investigating dust–pollutant interactions and assessing their environmental, climatic, and air-quality impacts.

Nevertheless, several limitations should be acknowledged. Because the observations were conducted within the lower atmospheric boundary layer, external mixing cannot be completely separated from chemical aging using lidar observations alone, and the lidar detects the fluorescence spectrum relatively narrowly, which is also an important limitation of this study. Although this range covers the main fluorescence features observed during the dust event, it cannot cover the entire emission spectrum. Therefore, it limits the ability to distinguish individual fluorescence substances and makes it difficult to differentiate the overlapping contributions of different organic compounds. Future studies should integrate lidar observations with offline chemical characterization, high-resolution mass spectrometry, and molecular biological analyzes to better identify the sources, compositions, and transformation pathways of fluorescent aerosols across different particle-size ranges. In addition, long-term observations conducted under diverse dust-source conditions and atmospheric environments are required to further evaluate the applicability, universality, and robustness of the DAI framework. Such efforts will help improve the interpretation of fluorescence-based aging indicators and enhance the application of lidar observations for investigating dust–pollutant interactions and aerosol chemical evolution.

CRediT authorship contribution statement

Yuanzong Ji: Writing – original draft, Visualization, Formal analysis, Data curation, Conceptualization. **Zhongwei Huang:** Investigation, Funding acquisition, Formal analysis, Conceptualization. **Yongkai Wang:** Writing – review & editing. **Wenjin Zhang:** Data curation. **Da Lu:** Data curation. **Qingqing Dong:** Data curation. **Jianrong Bi:** Data curation. **Tian Zhou:** Data curation.

Ethics declaration

The author(s) declare(s) that the study does not involve humans nor animal subjects.

Declaration of competing interest

The authors declare that they have no known competing financial interests or personal relationships that could have appeared to influence the work reported in this paper.

Acknowledgements

This work was supported by the National Natural Science Foundation of China (grant nos. 42427803 and W2411029), the Gansu Science and Technology Major Program (grant no. 24ZDWA006), the '111 Center' (B25040), and the Fundamental Research Funds for the Central Universities (grant no. lzujbky-2023-it09). We also greatly acknowledge the support of the Supercomputing Center of Lanzhou University, China.

Data availability

Data will be made available on request.

References

Ackerman, S.A., 1997. Remote sensing aerosols using satellite infrared observations. J. Geophys. Res. 102, 17069–17079. https://doi.org/10.1029/96JD03066.

Adebiyi, A., Kok, J.F., Murray, B.J., Ryder, C.L., Stuut, J.-B.W., Kahn, R.A., Knippertz, P., Formenti, P., Mahowald, N.M., Pérez García-Pando, C., Klose, M., Ansmann, A., Samset, B.H., Ito, A., Balkanski, Y., Di Biagio, C., Romanias, M.N., Huang, Y., Meng, J., 2023. A review of coarse mineral dust in the Earth system. Aeolian Res. 60, 100849. https://doi.org/10.1016/j.aeolia.2022.100849.

Afsana, S., Zhou, R., Miyazaki, Y., Tachibana, E., Deshmukh, D.K., Kawamura, K., Mochida, M., 2023. Fluorescence of solvent-extractable organics in sub-micrometer forest aerosols in Hokkaido, Japan. Atmos. Environ. 303, 119710. https://doi.org/10.1016/j.atmosenv.2023.119710.

Ansmann, A., Riebesell, M., Wandinger, U., Weitkamp, C., Voss, E., Lahmann, W., Michaelis, W., 1992. Combined Raman elastic-backscatter LIDAR for vertical profiling of moisture, aerosol extinction, backscatter, and LIDAR ratio. Appl. Phys. B Lasers Opt. 55, 18–28. https://doi.org/10.1007/BF00348608.

Aiyuk, M.B.E., Hoffmann, E.H., Tilgner, A., Wolke, R., Herrmann, H., 2024. A CAPRAM Modeling Study on the Role of Heterogeneous Reactions on Dust in Tropospheric Chemistry. ACS Earth Space Chem 8, 2052–2066. https://doi.org/10.1021/acsearthspacechem.4c00154.

Ansmann, A., Bösenberg, J., Chaikovsky, A., Comerón, A., Eckhardt, S., Eixmann, R., Freudenthaler, V., Ginoux, P., Komguem, L., Linné, H., Márquez, M.Á.L., Matthias, V., Mattis, I., Mitev, V., Müller, D., Music, S., Nickovic, S., Pelon, J., Sauvage, L., Sobolewsky, P., Srivastava, M.K., Stohl, A., Torres, O., Vaughan, G., Wandinger, U., Wiegner, M., 2003. Long-range transport of Saharan dust to northern Europe: the 11–16 October 2001 outbreak observed with EARLINET. J. Geophys. Res. 108, 4783. https://doi.org/10.1029/2003JD003757.

Avino, P., Manigrasso, M., 2017. Dynamic of submicrometer particles in urban environment. Environ. Sci. Pollut. Res. 24, 13908–13920. https://doi.org/10.1007/s11356-016-6752-8.

Bones, D.L., Henricksen, D.K., Mang, S.A., Gonsior, M., Bateman, A.P., Nguyen, T.B., Cooper, W.J., Nizkorodov, S.A., 2010. Appearance of strong absorbers and fluorophores in limonene-O3 secondary organic aerosol due to NH4+ −mediated

chemical aging over long time scales. J. Geophys. Res. 115, 2009JD012864. https://doi.org/10.1029/2009JD012864.
Brown, S.S., Stutz, J., 2012. Nighttime radical observations and chemistry. Chem. Soc. Rev. 41, 6405. https://doi.org/10.1039/c2cs35181a.
Carlton, A.G., Turpin, B.J., Altieri, K.E., Seitzinger, S., Reff, A., Lim, H.-J., Ervens, B., 2007. Atmospheric oxalic acid and SOA production from glyoxal: results of aqueous photooxidation experiments. Atmos. Environ. 41, 7588–7602. https://doi.org/10.1016/j.atmosenv.2007.05.035.
Casquero-Vera, J.A., Pérez-Ramírez, D., Lyamani, H., Rejano, F., Casans, A., Titos, G., Olmo, F.J., Dada, L., Hakala, S., Hussein, T., Lehtipalo, K., Paasonen, P., Hyvärinen, A., Pérez, N., Querol, X., Rodríguez, S., Kalivitis, N., González, Y., Alghamdi, M.A., Kerminen, V.-M., Alastuey, A., Petäjä, T., Alados-Arboledas, L., 2023. Impact of desert dust on new particle formation events and the cloud condensation nuclei budget in dust-influenced areas. Atmos. Chem. Phys. 23, 15795–15814. https://doi.org/10.5194/acp-23-15795-2023.
Chang, Y., Hu, Q., Goloub, P., Podvin, T., Veselovskii, I., Ducos, F., Dubois, G., Saito, M., Lopatin, A., Dubovik, O., Chen, C., 2025. Retrieval of microphysical properties of dust aerosols from extinction, backscattering and depolarization lidar measurements using various particle scattering models. Atmos. Chem. Phys. 25, 6787–6821. https://doi.org/10.5194/acp-25-6787-2025.
Chen, H., Navea, J.G., Young, M.A., Grassian, V.H., 2011. Heterogeneous photochemistry of trace atmospheric gases with components of mineral dust aerosol. J. Phys. Chem. A 115, 490–499. https://doi.org/10.1021/jp110164j.
Chen, G., Canonaco, F., Tobler, A., Aas, W., Alastuey, A., Allan, J., Atabakhsh, S., Aurela, M., Baltensperger, U., Bougiatioti, A., De Brito, J.F., Ceburnis, D., Chazeau, B., Chebaicheb, H., Daellenbach, K.R., Ehn, M., El Haddad, I., Eleftheriadis, K., Favez, O., Flentje, H., Font, A., Fossum, K., Freney, E., Gini, M., Green, D.C., Heikkinen, L., Herrmann, H., Kalogridis, A.-C., Keernik, H., Lhotka, R., Lin, C., Lunder, C., Maasikmets, M., Manousakas, M.I., Marchand, N., Marin, C., Marmureanu, L., Mihalopoulos, N., Močnik, G., Nęcki, J., O'Dowd, C., Ovadnevaite, J., Peter, T., Petit, J.-E., Pikridas, M., Matthew Platt, S., Pokorná, P., Poulain, L., Priestman, M., Riffault, V., Rinaldi, M., Różański, K., Schwarz, J., Sciare, J., Simon, L., Skiba, A., Slowik, J.G., Sosedova, Y., Stavroulas, I., Styszko, K., Teinemaa, E., Timonen, H., Tremper, A., Vasilescu, J., Via, M., Vodička, P., Wiedensohler, A., Zografou, O., Cruz Minguillón, M., Prévôt, A.S.H., 2022. European aerosol phenomenology − 8: harmonised source apportionment of organic aerosol using 22 year-long ACSM/AMS datasets. Environ. Int. 166, 107325. https://doi.org/10.1016/j.envint.2022.107325.
Chin, M., Kahn, R., 2009. Atmospheric aerosol properties and climate impacts. U.S. Climate Change Science Program.
Choobari, O.A., Zawar-Reza, P., Sturman, A., 2014. The global distribution of mineral dust and its impacts on the climate system: a review. Atmos. Res. 138, 152–165. https://doi.org/10.1016/j.atmosres.2013.11.007.
Coble, P.G., 1996. Characterization of marine and terrestrial DOM in seawater using excitation-emission matrix spectroscopy. Mar. Chem. 51, 325–346. https://doi.org/10.1016/0304-4203(95)00062-3.
Coquelin, L., Fischer, N., Motzkus, C., Mace, T., Gensdarmes, F., Brusquet, L.L., Fleury, G., 2013. Aerosol size distribution estimation and associated uncertainty for measurement with a scanning mobility particle sizer (SMPS). J. Phys. Conf. Ser. 429, 012018. https://doi.org/10.1088/1742-6596/429/1/012018.
Cwiertny, D.M., Young, M.A., Grassian, V.H., 2008. Chemistry and photochemistry of mineral dust aerosol. Annu. Rev. Phys. Chem. 59, 27–51. https://doi.org/10.1146/annurev.physchem.59.032607.093630.
Dai, C., Zhang, X., Lian, W., Wei, H., Liu, J., Zou, S., 2024. Comparison study between nitrate and sulfate aerosols and their coating effect on the scattering properties of mineral aerosol. Sci. Rep. 14, 21756. https://doi.org/10.1038/s41598-024-71532-x.
Deguillaume, L., Leriche, M., Desboeufs, K., Mailhot, G., George, C., Chaumerliac, N., 2005. Transition metals in atmospheric liquid phases: sources, reactivity, and sensitive parameters. Chem. Rev. 105, 3388–3431. https://doi.org/10.1021/cr040649c.
Dentener, F.J., Carmichael, G.R., Zhang, Y., Lelieveld, J., Crutzen, P.J., 1996. Role of mineral aerosol as a reactive surface in the global troposphere. J. Geophys. Res. 101, 22869–22889. https://doi.org/10.1029/96JD01818.
Ervens, B., Turpin, B.J., Weber, R.J., 2011. Secondary organic aerosol formation in cloud droplets and aqueous particles (aqSOA): a review of laboratory, field and model studies. Atmos. Chem. Phys. 11, 11069–11102. https://doi.org/10.5194/acp-11-11069-2011.
Fan, X., Cao, T., Yu, X., Wang, Y., Xiao, X., Li, F., Xie, Y., Ji, W., Song, J., Peng, P., 2020. The evolutionary behavior of chromophoric brown carbon during ozone aging of fine particles from biomass burning. Atmos. Chem. Phys. 20, 4593–4605. https://doi.org/10.5194/acp-20-4593-2020.
Farmer, D.K., Jimenez, J.L., 2010. Real-time atmospheric chemistry field instrumentation. Anal. Chem. 82, 7879–7884. https://doi.org/10.1021/ac1010603.
Fernald, F.G., 1984. Analysis of atmospheric lidar observations: some comments. Appl. Opt. 23, 652. https://doi.org/10.1364/AO.23.000652.
Finlayson-Pitts, B.J., Pitts, J.N., 2000. Chemistry of the upper and lower atmosphere: theory, experiments, and applications. Academic Press, San Diego. https://doi.org/10.1016/B978-0-12-257060-5.X5000-X.
Freudenthaler, V., Esselborn, M., Wiegner, M., Heese, B., Tesche, M., Ansmann, A., Müller, D., Althausen, D., Wirth, M., Fix, A., Ehret, G., Knippertz, P., Toledano, C., Gasteiger, J., Garhammer, M., Seefeldner, M., 2009. Depolarization ratio profiling at several wavelengths in pure Saharan dust during SAMUM 2006. Tellus Ser. B Chem. Phys. Meteorol. 61, 165. https://doi.org/10.1111/j.1600-0889.2008.00396.x.
Gaston, C.J., 2020. Re-examining dust chemical aging and its impacts on Earth's climate. Acc. Chem. Res. 53, 1005–1013. https://doi.org/10.1021/acs.accounts.0c00102.
Geng, H., Hwang, H., Liu, X., Dong, S., Ro, C.-U., 2014. Investigation of aged aerosols in size-resolved Asian dust storm particles transported from Beijing, China, to Incheon, Korea, using low- Z particle EPMA. Atmos. Chem. Phys. 14, 3307–3323. https://doi.org/10.5194/acp-14-3307-2014.
George, C., Ammann, M., D'Anna, B., Donaldson, D.J., Nizkorodov, S.A., 2015. Heterogeneous photochemistry in the atmosphere. Chem. Rev. 115, 4218–4258. https://doi.org/10.1021/cr500648z.
Goel, V., Mishra, S.K., Pal, P., Ahlawat, A., Vijayan, N., Jain, S., Sharma, C., 2020. Influence of chemical aging on physico-chemical properties of mineral dust particles: a case study of 2016 dust storms over Delhi. Environ. Pollut. 267, 115338. https://doi.org/10.1016/j.envpol.2020.115338.
Graber, E.R., Rudich, Y., 2006. Atmospheric HULIS: how humic-like are they? A comprehensive and critical review. Atmos. Chem. Phys. 6, 729–753. https://doi.org/10.5194/acp-6-729-2006.
Groß, S., Freudenthaler, V., Schepanski, K., Toledano, C., Schäfler, A., Ansmann, A., Weinzierl, B., 2015. Optical properties of long-range transported Saharan dust over Barbados as measured by dual-wavelength depolarization Raman lidar measurements. Atmos. Chem. Phys. 15, 11067–11080. https://doi.org/10.5194/acp-15-11067-2015.
Guo, H., Sullivan, A.P., Campuzano-Jost, P., Schroder, J.C., Lopez-Hilfiker, F.D., Dibb, J. E., Jimenez, J.L., Thornton, J.A., Brown, S.S., Nenes, A., Weber, R.J., 2016. Fine particle pH and the partitioning of nitric acid during winter in the northeastern United States. J. Geophys. Res. Atmos. 121. https://doi.org/10.1002/2016JD025311.
Haarig, M., Ansmann, A., Baars, H., Jimenez, C., Veselovskii, I., Engelmann, R., Althausen, D., 2018. Depolarization and lidar ratios at 355, 532, and 1064 nm and microphysical properties of aged tropospheric and stratospheric Canadian wildfire smoke. Atmos. Chem. Phys. 18, 11847–11861. https://doi.org/10.5194/acp-18-11847-2018.
Haywood, J.M., Abel, S.J., Barrett, P.A., Bellouin, N., Blyth, A., Bower, K.N., Brooks, M., Carslaw, K., Che, H., Coe, H., Cotterell, M.I., Crawford, I., Cui, Z., Davies, N., Dingley, B., Field, P., Formenti, P., Gordon, H., De Graaf, M., Herbert, R., Johnson, B., Jones, A.C., Langridge, J.M., Malavelle, F., Partridge, D.G., Peers, F., Redemann, J., Stier, P., Szpek, K., Taylor, J.W., Watson-Parris, D., Wood, R., Wu, H., Zuidema, P., 2021. The cloud–aerosol–radiation interaction and forcing: year 2017 (CLARIFY-2017) measurement campaign. Atmos. Chem. Phys. 21, 1049–1084. https://doi.org/10.5194/acp-21-1049-2021.
Huang, Z., Li, M., Bi, J., Shen, X., Zhang, S., Liu, Q., 2023. Small lidar ratio of dust aerosol observed by Raman-polarization lidar near desert sources. Opt. Express 31, 16909. https://doi.org/10.1364/OE.484501.
Huang, Z., Dong, Q., Zhou, T., Bi, J., Chen, R., Liu, Q., Abdullaev, S.F., Nozirov, D., Alam, K., Wang, T., Li, W., Li, Z., Song, X., Liu, W., 2025a. Vertical distribution, optical properties, and source attribution of summer dust in southern Tajikistan: ground-based observations and model results. Atmos. Environ. 361, 121514. https://doi.org/10.1016/j.atmosenv.2025.121514.
Huang, Z., Wang, Y., Zhou, T., Ji, Y., Bi, J., Shi, J., Wen, H., Huang, J., 2025b. Raman-polarization-fluorescence spectroscopic lidar for real-time detection of humic-like substance profiles. Environ. Sci. Technol. 59, 7235–7245. https://doi.org/10.1021/acs.est.5c00028.
Jiang, Y., Yang, H., Tan, W., Chen, S., Chen, H., Guo, P., Xu, Q., Gong, J., Yu, Y., 2024. Observation and classification of low-altitude haze aerosols using fluorescence–Raman–Mie polarization lidar in Beijing during spring 2024. Remote Sens. 16, 3225. https://doi.org/10.3390/rs16173225.
Jimenez, J.L., Canagaratna, M.R., Donahue, N.M., Prevot, A.S.H., Zhang, Q., Kroll, J.H., DeCarlo, P.F., Allan, J.D., Coe, H., Ng, N.L., Aiken, A.C., Docherty, K.S., Ulbrich, I. M., Grieshop, A.P., Robinson, A.L., Duplissy, J., Smith, J.D., Wilson, K.R., Lanz, V.A., Hueglin, C., Sun, Y.L., Tian, J., Laaksonen, A., Raatikainen, T., Rautiainen, J., Vaattovaara, P., Ehn, M., Kulmala, M., Tomlinson, J.M., Collins, D.R., Cubison, M.J., E., Dunlea, J., Huffman, J.A., Onasch, T.B., Alfarra, M.R., Williams, P.I., Bower, K., Kondo, Y., Schneider, J., Drewnick, F., Borrmann, S., Weimer, S., Demerjian, K., Salcedo, D., Cottrell, L., Griffin, R., Takami, A., Miyoshi, T., Hatakeyama, S., Shimono, A., Sun, J.Y., Zhang, Y.M., Dzepina, K., Kimmel, J.R., Sueper, D., Jayne, J. T., Herndon, S.C., Trimborn, A.M., Williams, L.R., Wood, E.C., Middlebrook, A.M., Kolb, C.E., Baltensperger, U., Worsnop, D.R., 2009. Evolution of organic aerosols in the atmosphere. Science 326, 1525–1529. https://doi.org/10.1126/science.1180353.
Jing, D., He, Y., Yin, Z., Liu, F., Yi, F., 2024. Long-term characteristics of dust aerosols over central China from 2010 to 2020 observed with polarization lidar. Atmos. Res. 297, 107129. https://doi.org/10.1016/j.atmosres.2023.107129.
Klingmüller, K., Karydis, V.A., Bacer, S., Stenchikov, G.L., Lelieveld, J., 2020. Weaker cooling by aerosols due to dust–pollution interactions. Atmos. Chem. Phys. 20, 15285–15295. https://doi.org/10.5194/acp-20-15285-2020.
Kok, Jasper F., 2011a. A scaling theory for the size distribution of emitted dust aerosols suggests climate models underestimate the size of the global dust cycle. Proc. Natl. Acad. Sci. USA 108, 1016–1021. https://doi.org/10.1073/pnas.1014798108.
Kok, J.F., 2011b. Does the size distribution of mineral dust aerosols depend on the wind speed at emission? Atmos. Chem. Phys. 11, 10149–10156. https://doi.org/10.5194/acp-11-10149-2011.
Kok, J.F., Storelvmo, T., Karydis, V.A., Adebiyi, A.A., Mahowald, N.M., Evan, A.T., He, C., Leung, D.M., 2023. Mineral dust aerosol impacts on global climate and climate change. Nat. Rev. Earth Environ. 4, 71–86. https://doi.org/10.1038/s43017-022-00379-5.
Kong, S., Sato, K., Bi, L., 2022. Lidar ratio–depolarization ratio relations of atmospheric dust aerosols: the super-spheroid model and high spectral resolution lidar observations. JGR-Atmos. 127, e2021JD035629. https://doi.org/10.1029/2021JD035629.

Laskin, A., Laskin, J., Nizkorodov, S.A., 2015. Chemistry of atmospheric brown carbon. Chem. Rev. 115, 4335–4382. https://doi.org/10.1021/cr5006167.
Lee, H.J. (Julie), Aiona, P.K., Laskin, A., Laskin, J., Nizkorodov, S.A., 2014. Effect of solar radiation on the optical properties and molecular composition of laboratory proxies of atmospheric brown carbon. Environ. Sci. Technol. 48, 10217–10226. https://doi.org/10.1021/es502515r.
Legrand, M., Plana-Fattori, A., N'doumé, C., 2001. Satellite detection of dust using the IR imagery of Meteosat: 1. Infrared difference dust index. J. Geophys. Res. 106, 18251–18274. https://doi.org/10.1029/2000JD900749.
Li, Y., Wang, W., 2024. Long-range transport of a dust event and impact on marine chlorophyll-a concentration in April 2023. Remote Sens. 16, 1883. https://doi.org/10.3390/rs16111883.
Li, B., Chen, S., Zhang, Y., Chen, H., Guo, P., 2019. Fluorescent aerosol observation in the lower atmosphere with an integrated fluorescence-Mie lidar. J. Quant. Spectrosc. Radiat. Transf. 227, 211–218. https://doi.org/10.1016/j.jqsrt.2019.02.019.
Li, W., Qi, Y., Qu, Wen, Qu, Wenjun, Shi, J., Zhang, D., Liu, Y., Wu, F., Ma, Yuanyuan, Zhang, Y., Ren, D., Du, X., Yang, S., Wang, X., Yi, L., Gao, X., Wang, W., Ma, Yingge, Sheng, L., Zhou, Y., 2023a. Sulfate and nitrate elevation in reverse-transport dust plumes over coastal areas of China. Atmos. Environ. 295, 119518. https://doi.org/10.1016/j.atmosenv.2022.119518.
Li, J., Zhang, N., Tian, P., Zhang, M., Shi, J., Chang, Y., Zhang, L., Liu, Z., Wang, Y., 2023b. Significant roles of aged dust aerosols on rapid nitrate formation under dry conditions in a semi-arid city. Environ. Pollut. 336, 122395. https://doi.org/10.1016/j.envpol.2023.122395.
Li, W., Ito, A., Wang, Guochen, Zhi, M., Xu, L., Yuan, Q., Zhang, J., Liu, L., Wu, F., Laskin, A., Zhang, D., Zhang, X., Zhu, T., Chen, J., Mihalopoulos, N., Bougiatioti, A., Kanakidou, M., Wang, Gehui, Hu, H., Zhao, Y., Shi, Z., 2025. Aqueous-phase secondary organic aerosol formation on mineral dust. Natl. Sci. Rev. 12, nwaf221. https://doi.org/10.1093/nsr/nwaf221.
Lim, Y.B., Tan, Y., Perri, M.J., Seitzinger, S.P., Turpin, B.J., 2010. Aqueous chemistry and its role in secondary organic aerosol (SOA) formation. Atmos. Chem. Phys. 10, 10521–10539. https://doi.org/10.5194/acp-10-10521-2010.
Liu, Z., Sugimoto, N., Murayama, T., 2002. Extinction-to-backscatter ratio of Asian dust observed with high-spectral-resolution lidar and Raman lidar. Appl. Opt. 41, 2760. https://doi.org/10.1364/AO.41.002760.
Liu, J., Zhang, F., Ren, J., Chen, L., Zhang, A., Wang, Z., Zou, S., Xu, H., Yue, X., 2025. The evolution of aerosol mixing state derived from a field campaign in Beijing: implications for particle aging timescales in urban atmospheres. Atmos. Chem. Phys. 25, 5075–5086. https://doi.org/10.5194/acp-25-5075-2025.
Lu, J., Shen, X., Ma, Q., Yu, A., Hu, X., Zhang, Y., Liu, Q., Liu, S., Che, H., Zhang, X., Sun, J., 2024. Size-resolved effective density of ambient aerosols measured by an AAC–SMPS tandem system in Beijing. Atmos. Environ. 318, 120226. https://doi.org/10.1016/j.atmosenv.2023.120226.
Lu, S.-J., Wang, D., Wang, Z., Li, B., Peng, Z.-R., Li, X.-B., Gao, Y., 2019. Investigating the Role of Meteorological Factors in the Vertical Variation in PM2.5 by Unmanned Aerial Vehicle Measurement. Aerosol Air Qual. Res. 19, 1493–1507. https://doi.org/10.4209/aaqr.2018.07.0266.
Luo, T., Wang, Z., Ferrare, R.A., Hostetler, C.A., Yuan, R., Zhang, D., 2015. Vertically resolved separation of dust and other aerosol types by a new lidar depolarization method. Opt. Express 23, 14095. https://doi.org/10.1364/OE.23.014095.
Mahowald, N., Jickells, T.D., Baker, A.R., Artaxo, P., Benitez-Nelson, C.R., Bergametti, G., Bond, T.C., Chen, Y., Cohen, D.D., Herut, B., Kubilay, N., Losno, R., Luo, C., Maenhaut, W., McGee, K.A., Okin, G.S., Siefert, R.L., Tsukuda, S., 2008. Global distribution of atmospheric phosphorus sources, concentrations and deposition rates, and anthropogenic impacts. Glob. Biogeochem. Cycles 22, 2008GB003240. https://doi.org/10.1029/2008GB003240.
Mao, R., Hu, Z., Chen, S., Feng, T., 2026. Editorial: dust and polluted aerosols: sources, transport and radiative effects volume II. Front. Environ. Sci. 13, 1762418. https://doi.org/10.3389/fenvs.2025.1762418.
Meng, Z., Xing, Y., Zhang, X., Niu, S., Tian, W., Zhang, Q., 2024. Chemical characteristics and health risk assessment of fine particulate matter from typical emission source in Xi'an, Northwestern China. Aerosol Sci. Eng. 8, 468–481. https://doi.org/10.1007/s41810-024-00235-7.
Miyamoto, C., Sakata, K., Yamakawa, Y., Takahashi, Y., 2020. Determination of calcium and sulfate species in aerosols associated with the conversion of its species through reaction processes in the atmosphere and its influence on cloud condensation nuclei activation. Atmos. Environ. 223, 117193. https://doi.org/10.1016/j.atmosenv.2019.117193.
Müller, D., Ansmann, A., Mattis, I., Tesche, M., Wandinger, U., Althausen, D., Pisani, G., 2007. Aerosol-type-dependent lidar ratios observed with Raman lidar. J. Geophys. Res. 112, 2006JD008292. https://doi.org/10.1029/2006JD008292.
Nannu Shankar, S., Mital, K., Le, E., Lewis, G.S., Eiguren-Fernandez, A., Sabo-Attwood, T., Wu, C.-Y., 2023. Assessment of scanning mobility particle sizer (SMPS) for online monitoring of delivered dose in an in vitro aerosol exposure system. Toxicol. in Vitro 92, 105650. https://doi.org/10.1016/j.tiv.2023.105650.
Ng, N.L., Canagaratna, M.R., Zhang, Q., Jimenez, J.L., Tian, J., Ulbrich, I.M., Kroll, J.H., Docherty, K.S., Chhabra, P.S., Bahreini, R., Murphy, S.M., Seinfeld, J.H., Hildebrandt, L., Donahue, N.M., DeCarlo, P.F., Lanz, V.A., Prévôt, A.S.H., Dinar, E., Rudich, Y., Worsnop, D.R., 2010. Organic aerosol components observed in Northern Hemispheric datasets from aerosol mass spectrometry. Atmos. Chem. Phys. 10, 4625–4641. https://doi.org/10.5194/acp-10-4625-2010.
Ng, N.L., Brown, S.S., Archibald, A.T., Atlas, E., Cohen, R.C., Crowley, J.N., Day, D.A., Donahue, N.M., Fry, J.L., Fuchs, H., Griffin, R.J., Guzman, M.I., Herrmann, H., Hodzic, A., Iinuma, Y., Jimenez, J.L., Kiendler-Scharr, A., Lee, B.H., Luecken, D.J., Mao, J., McLaren, R., Mutzel, A., Osthoff, H.D., Ouyang, B., Picquet-Varrault, B., Platt, U., Pye, H.O.T., Rudich, Y., Schwantes, R.H., Shiraiwa, M., Stutz, J., Thornton, J.A., Tilgner, A., Williams, B.J., Zaveri, R.A., 2017. Nitrate radicals and biogenic volatile organic compounds: oxidation, mechanisms, and organic aerosol. Atmos. Chem. Phys. 17, 2103–2162. https://doi.org/10.5194/acp-17-2103-2017.
Pan, Y.-L., 2015. Detection and characterization of biological and other organic-carbon aerosol particles in atmosphere using fluorescence. J. Quant. Spectrosc. Radiat. Transf. 150, 12–35. https://doi.org/10.1016/j.jqsrt.2014.06.007.
Pan, Y.-L., Hill, S.C., Santarpia, J.L., Brinkley, K., Sickler, T., Coleman, M., Williamson, C., Gurton, K., Felton, M., Pinnick, R.G., Baker, N., Eshbaugh, J., Hahn, J., Smith, E., Alvarez, B., Prugh, A., Gardner, W., 2014. Spectrally-resolved fluorescence cross sections of aerosolized biological live agents and simulants using five excitation wavelengths in a BSL-3 laboratory. Opt. Express 22, 8165. https://doi.org/10.1364/OE.22.008165.
Pan, X., Uno, I., Wang, Zhe, Nishizawa, T., Sugimoto, N., Yamamoto, S., Kobayashi, H., Sun, Y., Fu, P., Tang, X., Wang, Zifa, 2017. Real-time observational evidence of changing Asian dust morphology with the mixing of heavy anthropogenic pollution. Sci. Rep. 7, 335. https://doi.org/10.1038/s41598-017-00444-w.
Papetta, A., Kezoudi, M., Baars, H., Floutsi, A., Drakaki, E., Kandler, K., Louca, E., Christoudias, T., Marinou, E., Stopford, C., Thornberry, T., Amiridis, V., Sciare, J., Marenco, F., 2025. Volume-to-Extinction Ratio: An Important Property of Dust. https://doi.org/10.5194/egusphere-2025-3404.
Pinder, R.W., Adams, P.J., Pandis, S.N., 2007. Ammonia emission controls as a cost-effective strategy for reducing atmospheric particulate matter in the Eastern United States. Environ. Sci. Technol. 41, 380–386. https://doi.org/10.1021/es060379a.
Pöhlker, C., Huffman, J.A., Pöschl, U., 2012. Autofluorescence of atmospheric bioaerosols – fluorescent biomolecules and potential interferences. Atmos. Meas. Tech. 5, 37–71. https://doi.org/10.5194/amt-5-37-2012.
Polymenakou, P.N., Mandalakis, M., Stephanou, E.G., Tselepides, A., 2008. Particle size distribution of airborne microorganisms and pathogens during an intense African dust event in the Eastern Mediterranean. Environ. Health Perspect. 116, 292–296. https://doi.org/10.1289/ehp.10684.
Pye, H.O.T., Nenes, A., Alexander, B., Ault, A.P., Barth, M.C., Clegg, S.L., Collett Jr., J.L., Fahey, K.M., Hennigan, C.J., Herrmann, H., Kanakidou, M., Kelly, J.T., Ku, I.-T., McNeill, V.F., Riemer, N., Schaefer, T., Shi, G., Tilgner, A., Walker, J.T., Wang, T., Weber, R., Xing, J., Zaveri, R.A., Zuend, A., 2020. The acidity of atmospheric particles and clouds. Atmos. Chem. Phys. 20, 4809–4888. https://doi.org/10.5194/acp-20-4809-2020.
Qin, J., Tan, J., Zhou, X., Yang, Y., Qin, Y., Wang, Xiaobo, Shi, S., Xiao, K., Wang, Xinming, 2022. Measurement report: particle-size-dependent fluorescence properties of water-soluble organic compounds (WSOCs) and their atmospheric implications for the aging of WSOCs. Atmos. Chem. Phys. 22, 465–479. https://doi.org/10.5194/acp-22-465-2022.
Reichardt, J., Behrendt, O., Lauermann, F., 2023. Spectrometric fluorescence and Raman lidar: absolute calibration of aerosol fluorescence spectra and fluorescence correction of humidity measurements. Atmos. Meas. Tech. 16, 1–13. https://doi.org/10.5194/amt-16-1-2023.
Reichardt, J., Lauermann, F., Behrendt, O., 2025. Fluorescence spectra of atmospheric aerosols. Atmos. Chem. Phys. 25, 5857–5892. https://doi.org/10.5194/acp-25-5857-2025.
Reid, J.S., Kinney, J.E., Westphal, D.L., Holben, B.N., Welton, E.J., Tsay, S., Eleuterio, D. P., Campbell, J.R., Christopher, S.A., Colarco, P.R., Jonsson, H.H., Livingston, J.M., Maring, H.B., Meier, M.L., Pilewskie, P., Prospero, J.M., Reid, E.A., Remer, L.A., Russell, P.B., Savoie, D.L., Smirnov, A., Tanré, D., 2003. Analysis of measurements of Saharan dust by airborne and ground-based remote sensing methods during the Puerto Rico dust experiment (PRIDE). J. Geophys. Res. 108, 2002JD002493. https://doi.org/10.1029/2002JD002493.
Richardson, S.C., Mytilinaios, M., Foskinis, R., Kyrou, C., Papayannis, A., Pyrri, I., Giannoutsou, E., Adamakis, I.D.S., 2019. Bioaerosol detection over Athens, Greece using the laser induced fluorescence technique. Sci. Total Environ. 696, 133906. https://doi.org/10.1016/j.scitotenv.2019.133906.
Rückerl, R., Schneider, A., Breitner, S., Cyrys, J., Peters, A., 2011. Health effects of particulate air pollution: a review of epidemiological evidence. Inhal. Toxicol. 23, 555–592. https://doi.org/10.3109/08958378.2011.593587.
Sakai, T., Nagai, T., Zaizen, Y., Mano, Y., 2010. Backscattering linear depolarization ratio measurements of mineral, sea-salt, and ammonium sulfate particles simulated in a laboratory chamber. Appl. Opt. 49, 4441. https://doi.org/10.1364/AO.49.004441.
Santos, P.S.M., Otero, M., Duarte, R.M.B.O., Duarte, A.C., 2009. Spectroscopic characterization of dissolved organic matter isolated from rainwater. Chemosphere 74, 1053–1061. https://doi.org/10.1016/j.chemosphere.2008.10.061.
Seinfeld, J.H., Pandis, S.N., 2016. Atmospheric Chemistry and Physics: From Air Pollution to Climate Change, Third edition. John Wiley & Sons, Inc, Hoboken, New Jersey.
Shang, X., Filioglou, M., Hofer, J., Haarig, M., Hu, Q., Goloub, P., Romakkaniemi, S., Komppula, M., 2026. Decomposition of three aerosol types using lidar-derived depolarization ratios at two wavelengths. Atmos. Meas. Tech. 19, 679–697. https://doi.org/10.5194/amt-19-679-2026.
Shao, Y., Wyrwoll, K.-H., Chappell, A., Huang, J., Lin, Z., McTainsh, G.H., Mikami, M., Tanaka, T.Y., Wang, X., Yoon, S., 2011. Dust cycle: an emerging core theme in Earth system science. Aeolian Res. 2, 181–204. https://doi.org/10.1016/j.aeolia.2011.02.001.
Shen, X., Zhao, Y., Chen, Z., Huang, D., 2013. Heterogeneous reactions of volatile organic compounds in the atmosphere. Atmos. Environ. 68, 297–314. https://doi.org/10.1016/j.atmosenv.2012.11.027.
Shin, S.-K., Müller, D., Lee, C., Lee, K.H., Shin, D., Kim, Y.J., Noh, Y.M., 2015. Vertical variation of optical properties of mixed Asian dust/pollution plumes according to pathway of air mass transport over East Asia. Atmos. Chem. Phys. 15, 6707–6720. https://doi.org/10.5194/acp-15-6707-2015.

Sierra, M.M.D., Giovanela, M., Parlanti, E., Soriano-Sierra, E.J., 2005. Fluorescence fingerprint of fulvic and humic acids from varied origins as viewed by single-scan and excitation/emission matrix techniques. Chemosphere 58, 715–733. https://doi.org/10.1016/j.chemosphere.2004.09.038.

Song, Y.-C., Eom, H.-J., Jung, H.-J., Malek, M.A., Kim, H.K., Geng, H., Ro, C.-U., 2013. Investigation of aged Asian dust particles by the combined use of quantitative ED-EPMA and ATR-FTIR imaging. Atmos. Chem. Phys. 13, 3463–3480. https://doi.org/10.5194/acp-13-3463-2013.

Sugimoto, N., Lee, C.H., 2006. Characteristics of dust aerosols inferred from lidar depolarization measurements at two wavelengths. Appl. Opt. 45, 7468. https://doi.org/10.1364/AO.45.007468.

Sugimoto, N., Huang, Z., Nishizawa, T., Matsui, I., Tatarov, B., 2012a. Fluorescence from atmospheric aerosols observed with a multi-channel lidar spectrometer. Opt. Express 20, 20800. https://doi.org/10.1364/OE.20.020800.

Sugimoto, N., Huang, Z., Nishizawa, T., Matsui, I., Tatarov, B., 2012b. Study of fluorescence of atmospheric aerosols using a lidar spectrometer. In: Asai, K., Sugimoto, N., Singh, U.N., Jayaraman, A., Huang, J., Mueller, D. (Eds.), Presented at the SPIE Asia-Pacific Remote Sensing, Kyoto, Japan, p. 852607. https://doi.org/10.1117/12.977177.

Sugimoto, N., Nishizawa, T., Shimizu, A., Matsui, I., Kobayashi, H., 2015. Detection of internally mixed Asian dust with air pollution aerosols using a polarization optical particle counter and a polarization-sensitive two-wavelength lidar. J. Quant. Spectrosc. Radiat. Transf. 150, 107–113. https://doi.org/10.1016/j.jqsrt.2014.08.003.

Sugimoto, N., Shimizu, A., Matsui, I., Nishikawa, M., 2016. A method for estimating the fraction of mineral dust in particulate matter using PM2.5-to-PM10 ratios. Particuology 28, 114–120. https://doi.org/10.1016/j.partic.2015.09.005.

Tang, M., Huang, X., Lu, K., Ge, M., Li, Y., Cheng, P., Zhu, T., Ding, A., Zhang, Y., Gligorovski, S., Song, W., Ding, X., Bi, X., Wang, X., 2017. Heterogeneous reactions of mineral dust aerosol: implications for tropospheric oxidation capacity. Atmos. Chem. Phys. 17, 11727–11777. https://doi.org/10.5194/acp-17-11727-2017.

Tang, D., Li, Z., Xia, H., 2025. Clustering of weak fluorescence spectra from bioaerosol in air using laser-induced fluorescence lidar. Opt. Express 33, 24396. https://doi.org/10.1364/OE.560805.

Tesche, M., Ansmann, A., Müller, D., Althausen, D., Mattis, I., Heese, B., Freudenthaler, V., Wiegner, M., Esselborn, M., Pisani, G., Knippertz, P., 2009. Vertical profiling of Saharan dust with Raman lidars and airborne HSRL in southern Morocco during SAMUM. Tellus Ser. B Chem. Phys. Meteorol. 61, 144. https://doi.org/10.1111/j.1600-0889.2008.00390.x.

Tian, Y., Pan, X., Nishizawa, T., Kobayashi, H., Uno, I., Wang, X., Shimizu, A., Wang, Z., 2018. Variability of depolarization of aerosol particles in the megacity of Beijing: implications for the interaction between anthropogenic pollutants and mineral dust particles. Atmos. Chem. Phys. 18, 18203–18217. https://doi.org/10.5194/acp-18-18203-2018.

Tong, H., Lakey, P.S.J., Arangio, A.M., Socorro, J., Shen, F., Lucas, K., Brune, W.H., Pöschl, U., Shiraiwa, M., 2018. Reactive oxygen species formed by secondary organic aerosols in water and surrogate lung fluid. Environ. Sci. Technol., acs.est.8b03695 https://doi.org/10.1021/acs.est.8b03695.

Usher, C.R., Michel, A.E., Grassian, V.H., 2003. Reactions on mineral dust. Chem. Rev. 103, 4883–4940. https://doi.org/10.1021/cr020657y.

Veselovskii, I., Hu, Q., Goloub, P., Podvin, T., Korenskiy, M., Pujol, O., Dubovik, O., Lopatin, A., 2020. Combined use of Mie–Raman and fluorescence lidar observations for improving aerosol characterization: feasibility experiment. Atmos. Meas. Tech. 13, 6691–6701. https://doi.org/10.5194/amt-13-6691-2020.

Wang, Zhe, Pan, X., Uno, I., Li, J., Wang, Zifa, Chen, X., Fu, P., Yang, T., Kobayashi, H., Shimizu, A., Sugimoto, N., Yamamoto, S., 2017. Significant impacts of heterogeneous reactions on the chemical composition and mixing state of dust particles: a case study during dust events over northern China. Atmos. Environ. 159, 83–91. https://doi.org/10.1016/j.atmosenv.2017.03.044.

Wang, W., Gong, W., Mao, F., Pan, Z., 2018a. Physical constraint method to determine optimal overlap factor of Raman lidar. J. Opt. 47, 83–90. https://doi.org/10.1007/s12596-017-0427-9.

Wang, T., Liu, Y., Deng, Y., Fu, H., Zhang, L., Chen, J., 2018b. Emerging investigator series: heterogeneous reactions of sulfur dioxide on mineral dust nanoparticles: from single component to mixed components. Environ. Sci. Nano 5, 1821–1833. https://doi.org/10.1039/C8EN00376A.

Wang, Y., Huang, Z., Zhou, T., Bi, J., Shi, J., 2023a. Identification of fluorescent aerosol observed by a spectroscopic lidar over Northwest China. Opt. Express 31, 22157. https://doi.org/10.1364/OE.493557.

Wang, X., Wang, Q., Prass, M., Pöhlker, C., Moran-Zuloaga, D., Artaxo, P., Gu, J., Yang, N., Yang, X., Tao, J., Hong, J., Ma, N., Cheng, Y., Su, H., Andreae, M.O., 2023b. The export of African mineral dust across the Atlantic and its impact over the Amazon Basin. Atmos. Chem. Phys. 23, 9993–10014. https://doi.org/10.5194/acp-23-9993-2023.

Wang, W., Zhou, H., Gao, Y., Lyu, R., Xing, J., Zhou, X., Li, X., Shao, L., 2024. Morphology and chemical composition of mineral particles in a special dust storm with high relative humidity in North China. Environ. Technol. Innovation 36, 103823. https://doi.org/10.1016/j.eti.2024.103823.

Weinzierl, B., Petzold, A., Esselborn, M., Wirth, M., Rasp, K., Kandler, K., Schütz, L., Koepke, P., Fiebig, M., 2009. Airborne measurements of dust layer properties, particle size distribution and mixing state of Saharan dust during SAMUM 2006. Tellus Ser. B Chem. Phys. Meteorol. 61, 96. https://doi.org/10.1111/j.1600-0889.2008.00392.x.

Welton, E.J., Campbell, J.R., 2002. Micropulse lidar signals: uncertainty analysis. J. Atmos. Ocean. Technol. 19, 2089–2094. https://doi.org/10.1175/1520-0426(2002)019%253C2089:MLSUA%253E2.0.CO;2.

Wong, C., Vuong, J., Nizkorodov, S.A., 2024. Biogenic and anthropogenic secondary organic aerosols become fluorescent after highly acidic aging. J. Phys. Chem. A 128, 7657–7668. https://doi.org/10.1021/acs.jpca.4c04287.

Wu, T., Boor, B.E., 2021. Urban aerosol size distributions: a global perspective. Atmos. Chem. Phys. 21, 8883–8914. https://doi.org/10.5194/acp-21-8883-2021.

Xie, M., Mladenov, N., Williams, M.W., Neff, J.C., Wasswa, J., Hannigan, M.P., 2016. Water soluble organic aerosols in the Colorado Rocky Mountains, USA: composition, sources and optical properties. Sci. Rep. 6, 39339. https://doi.org/10.1038/srep39339.

Yadav, A.C., Tatarov, B., Song, R., Ghita, A., Müller, D., 2025. Characterizing the Saharan dust transported to the UK through lidar ratio, particle depolarization, and spectroscopic measurements. Atmos. Environ. 363, 121613. https://doi.org/10.1016/j.atmosenv.2025.121613.

Yang, L., Zhang, S., Tao, H., Yang, Y., Wang, L., Cui, Y., Xu, Y., Li, X., 2022. Comprehensive Analysis of a Dust Storm by a Lidar Network Combined With Multiple Data. Front. Environ. Sci. 10, 832710. https://doi.org/10.3389/fenvs.2022.832710.

Yao, W., Zhang, Y., Pan, X., Liu, H., Ye, J., Lv, S., Li, S., Sun, Y., Xin, J., Su, H., Wang, Z., 2026. Revealing the evolution of aerosols in Asian dust events: insights from their microphysical and elemental characteristics. J. Environ. Sci. 165, 579–588. https://doi.org/10.1016/j.jes.2025.08.009.

Zan, J., Maher, B.A., Fang, X., Stevens, T., Ning, W., Wu, F., Yang, Y., Kang, J., Hu, Z., 2025. Global dust impacts on biogeochemical cycles and climate. Nat. Rev. Earth Environ. 6, 789–807. https://doi.org/10.1038/s43017-025-00734-2.

Zhang, Q., Jimenez, J.L., Canagaratna, M.R., Allan, J.D., Coe, H., Ulbrich, I., Alfarra, M. R., Takami, A., Middlebrook, A.M., Sun, Y.L., Dzepina, K., Dunlea, E., Docherty, K., DeCarlo, P.F., Salcedo, D., Onasch, T., Jayne, J.T., Miyoshi, T., Shimono, A., Hatakeyama, S., Takegawa, N., Kondo, Y., Schneider, J., Drewnick, F., Borrmann, S., Weimer, S., Demerjian, K., Williams, P., Bower, K., Bahreini, R., Cottrell, L., Griffin, R.J., Rautiainen, J., Sun, J.Y., Zhang, Y.M., Worsnop, D.R., 2007. Ubiquity and dominance of oxygenated species in organic aerosols in anthropogenically-influenced Northern Hemisphere midlatitudes. Geophys. Res. Lett. 34, 2007GL029979. https://doi.org/10.1029/2007GL029979.

Zhang, R., Khalizov, A.F., Pagels, J., Zhang, D., Xue, H., McMurry, P.H., 2008. Variability in morphology, hygroscopicity, and optical properties of soot aerosols during atmospheric processing. Proc. Natl. Acad. Sci. USA 105, 10291–10296. https://doi.org/10.1073/pnas.0804860105.

Zhang, G., Bi, X., Li, L., Chan, L.Y., Li, M., Wang, X., Sheng, G., Fu, J., Zhou, Z., 2013. Mixing state of individual submicron carbon-containing particles during spring and fall seasons in urban Guangzhou, China: a case study. Atmos. Chem. Phys. 13, 4723–4735. https://doi.org/10.5194/acp-13-4723-2013.

Zhang, M., Su, H., Li, G., Kuhn, U., Li, S., Klimach, T., Hoffmann, T., Fu, P., Pöschl, U., Cheng, Y., 2021a. High-resolution fluorescence spectra of airborne biogenic secondary organic aerosols: comparisons to primary biological aerosol particles and implications for single-particle measurements. Environ. Sci. Technol. 55, 16747–16756. https://doi.org/10.1021/acs.est.1c02536.

Zhang, Y., Sun, Z., Chen, Siying, Chen, H., Guo, P., Chen, Su, He, J., Wang, J., Nian, X., 2021b. Classification and source analysis of low-altitude aerosols in Beijing using fluorescence–Mie polarization lidar. Opt. Commun. 479, 126417. https://doi.org/10.1016/j.optcom.2020.126417.

Zhang, S., Huang, Z., Li, M., Shen, X., Wang, Y., Dong, Q., Bi, J., Zhang, J., Li, W., Li, Z., Song, X., 2022a. Vertical structure of dust aerosols observed by a ground-based Raman lidar with polarization capabilities in the center of the Taklimakan Desert. Remote Sens. 14, 2461. https://doi.org/10.3390/rs14102461.

Zhang, X., Wei, H., Zou, S., Duan, J., Li, W., Dai, C., 2022b. Effect of nitrate coatings on the optical properties of mineral dust particles during the haze aging process. J. Quant. Spectrosc. Radiat. Transf. 277, 107966. https://doi.org/10.1016/j.jqsrt.2021.107966.

Zhang, X.-X., Yang, X.-H., Yang, F., Lei, J.-Q., Ali, M., Li, S.-Y., Liu, L.-Y., Xue, Y.-B., Wang, Z.-F., Tian, W.-J., Wang, Y.-D., Tang, X., 2025. Windblown dust in the Tarim basin, Northwest China. Sci. Rep. 15, 11209. https://doi.org/10.1038/s41598-025-95974-z.

Zhao, J., Zhang, F., Xu, Y., Chen, J., Yin, L., Shang, X., Xu, L., 2011. Chemical characteristics of particulate matter during a heavy dust episode in a Coastal City, Xiamen, 2010. Aerosol Air Qual. Res. 11, 299–308. https://doi.org/10.4209/aaqr.2010.09.0073.